# Plastic Anisotropy Evolution of SS316L and Modeling for Novel Cruciform Specimen

by

Elizabeth M. Mamros[a], Sarah M. Mayer[a], Dilip K. Banerjee[b], Mark A. Iadicola[b],

Brad L. Kinsey[a], Jinjin Ha[a]*

* Corresponding author: jinjin.ha@unh.edu (+1-603-862-5469)

April 2022

[a] Department of Mechanical Engineering, University of New Hampshire

33 Academic Way, Durham, NH 03824, USA

elizabeth.mamros@unh.edu, sarah.mayer@unh.edu, brad.kinsey@unh.edu

[b] Material Measurement Laboratory, National Institute of Standards and Technology (NIST)

100 Bureau Drive, STOP 8550, Gaithersburg, MD 20899, USA

dilip.banerjee@nist.gov, mark.iadicola@nist.gov

**Abstract**

In this paper, the evolution of the plastic anisotropy of stainless steel 316L samples is investigated under proportional loading paths using a customized cruciform specimen. The determination of a novel cruciform specimen by a design of experiments approach integrated with finite element simulations is described. The mechanical properties of the material are characterized under uniaxial tension applied in every 15$^{o}$ from the rolling direction and equibiaxial tension from hydraulic bulge experiments. The results reveal that the plastic anisotropy shown in stress and strain significantly evolves with respect to the plastic work. Based on the experiments, the material behavior is modeled using a non-quadratic anisotropic yield function, Yld2004-18p, with parameters modeled as a function of the equivalent plastic strain assuming plastic work equivalence and with constant parameters for comparison. The Hockett-Sherby model is also used for the strain hardening behavior to extrapolate the results to higher strain values. The models are implemented into a user material subroutine for finite element simulations. To validate the model, in-plane biaxial tension experiments are performed, using a customized specimen, to achieve greater deformation than previous designs by introducing double-sided pockets for thickness reduction and notches in the corner areas. The results are compared with finite element simulations implemented with the plasticity models.

**Keywords:** B. anisotropic material, B. constitutive behavior, B. elastic-plastic material, C. finite elements, C. mechanical testing

## 1. Introduction

Building accurate material models often involves the consideration of various aspects of material behavior, one of which is differences with respect to the material orientation, so called plastic anisotropy, of sheet metals. In terms of mechanical behavior, plastic anisotropy is often defined by ratios in stress and strain with respect to a reference. The values are not unity, i.e., non-isotropic, in general and can be varied with the material orientation. Their numerical formulations, so called anisotropic yield functions, have been published in the past 75 years starting with Hill and Orowan [1], who published a yield function for orthotropic materials based on the isotropic von Mises yield function in 1948. Several years later, Hosford [2] derived a generalized yield function based on the isotropic yield function from Hershey [3]. Barlat and Lian [4] modified Hosford's yield function to incorporate the effect of shear stress. In the decades since, increasingly advanced yield functions, e.g., Karafillis and Boyce [5], Barlat family functions [6–9], Cazacu and Barlat [10,11], Bron and Besson [12], and Banabic, Balan, and Comsa (BBC) family functions [13,14], have been developed to improve plastic anisotropy predictions, some of which are summarized in the reviews by Banabic et al. [15] and Barlat and Kuwabara [16].

These recent developments have proven successful in their ability to simulate forming processes for a material of consistent plastic anisotropy during deformation [17–21], i.e., relatively constant stress ratios and r-values with respect to plastic work. However, for some materials, a clear distinction is observed in the plastic anisotropy at different levels of plastic work under non-proportional [22–24] or proportional loading [18,25]. The former often presents strong evolutions in the anisotropy, especially upon the loading path change, with respect to plastic work. Thus, it is modeled in conjunction

with kinematic [26–28] or distortional hardening models [29–31], which can capture Bauschinger effect, permanent softening, latent hardening effect, etc., depending on the material. In contrast, the latter presents relatively minor plastic anisotropy changes primarily caused by the texture evolution during deformation [25]. To model this, as an example, Kuwabara et al. [25] calibrated an exponential function, using data at several strain levels, for each parameter of Yld2000-2d [8]. When choosing a yield function, specific types of metals, e.g., steel [30,32,33], aluminum [21,34–37], titanium [38–40], magnesium [41,42] alloys, etc., and their textures can be considered to provide an adequate description of plastic anisotropy. Simultaneously, the computational expense in numerical simulations, which results from the complexity of the model necessitated by the desired level of accuracy, must be balanced.

These advanced plasticity models often require the identification of more parameters, and thus basic material characterization experiments, e.g., uniaxial tension, are insufficient, especially for modeling forming processes. These modeling efforts may be further complicated by the inclusion of stress superposition [43], varying deformation paths [27,44–47], and ductile damage and fracture analysis [48,49]. In 1967, Shiratori and Ikegami [50] designed four potential cruciform specimen geometries and conducted biaxial tension experiments to study more complex deformations. Later, Kuwabara et al. [51] proposed a cruciform specimen with straight arms and investigated the work hardening in cold-rolled steel under biaxial tension. In the decades since, many cruciform geometries have been proposed, one of which is designated as ISO standard 16842 [52] (see more information in [51,53–55]), but an ASTM standard does not exist.

In Banerjee et al. [56], the criteria cited most often for designing cruciform biaxial specimens are uniformity of strain fields, minimization of shear strains, failure behavior in the gauge area, and reduced stress concentrations outside the major deformation region. Common strategies for achieving these objectives include creating notches at the corners [57,58], reducing or increasing the thickness in specific regions [59–61], machining slots in the arms [51,52,59], or some combination thereof [62]. Deng et al. [59] proposed a modified design with a reduced thickness area that does not require inverse numerical calibration and presented the yield locus of a dual-phase steel, DP590, determined experimentally using the specimen. Murakoso and Kuwabara [63] used cruciform specimens to analyze ultra-thin stainless steel sheets under biaxial tension. Despite numerous specimen designs already available in the literature [64], additional variations are still being generated to tailor the achievable results and place emphasis on certain design specifications according to the authors' intended applications. For example, the predecessors to the geometry described in this work required a sufficiently large gauge area for material characterization, such as strain measurement and microstructure imaging [65,66].

For material modeling purposes, the addition of in-plane biaxial cruciform experiments is beneficial for parameter identification or validation of models calibrated using conventional experiments, such as uniaxial tension in different orientations. Although the available testing conditions of in-plane biaxial experiments are mostly limited to the biaxial tension stress states, compression combined with tension [67] can be applied with additional equipment, e.g., an anti-buckling device. Alternatively, shear combined with tension [68] or plane strain tension [69] can be investigated with custom

geometries. A custom device with hinged fixtures and knife-edges has also been developed for off-axes testing [70]. These experiments can improve specific aspects of the material models required by numerical analyses. In Steglich et al. [41], AZ31 magnesium alloy biaxial deformation experiments were used to validate a visco-plastic self-consistent model. In Kuwabara et al. [25], 6016-O and 6016-T4 aluminum alloys were compared experimentally and numerically using cruciform specimens to determine the effects of heat treatment on the plastic anisotropy. In addition to plasticity modeling, Leotoing et al. [71,72] performed in-plane biaxial experiments to investigate the non-linear prestraining effect and construct numerical forming limit models. Ha et al. [36] used a specialized cruciform specimen, in conjunction with center-hole and shear specimens, to characterize the ductile fracture of a heat treated aluminum alloy, AA6111, using the experimental-numerical hybrid method. Kuwabara et al. [73] used the ISO standard cruciform geometry in comparison to uniaxial compression experiments to characterize the strength differential effect in a low carbon steel. Additionally, a 0.8 mm-thick mild steel cruciform specimen using the ISO standard geometry was measured up to a plastic strain level of 0.234 in non-linear stress path experiments to validate the material model [74].

In this paper, the evolution of plastic anisotropy in stainless steel 316L (SS316L) under proportional loading is investigated using a newly designed cruciform specimen and advanced material modeling for the numerical simulation. The plasticity characterization is presented in Section 2 with the experimental results of uniaxial and equibiaxial tensions. Based on the experiments, the material is modeled in Section 3 using a non-quadratic anisotropic yield function with equivalent plastic strain dependent parameters, i.e., Yld2004-18p ($\bar{\varepsilon}$), and Hockett-Sherby strain hardening. Section 4

describes the optimization of the cruciform geometry based on six design goals and the in-plane biaxial experiments using the determined cruciform specimen under four proportional loading conditions. In Section 5, finite element (FE) simulations of the cruciform experiments are performed, using Yld2004-18p($\bar{\varepsilon}$), Yld2004-18p with constant parameters, and von Mises yield functions, and compared to experimental results to validate the implemented models under the given loading conditions. The work is summarized with conclusions in Section 6.

## 2. Plasticity characterization

For the material characterization of SS316L sheet of 1.2 mm thickness, uniaxial and equibiaxial tension experiments were performed. From these experimental results, the strain ratios and normalized stresses are calculated at seven plastic work levels to evaluate the plastic anisotropy evolution. Refer to Table 1 for a summary of the material characterization results.

### 2.1. Uniaxial tension experiment

Seven uniaxial tension experiments were conducted using the ASTM E8 standard sheet-type specimen [75] oriented every 15° from the rolling direction (RD) to the transverse direction (TD) at room temperature in displacement control (5 mm/min), which corresponds to a static strain rate ($\dot{\varepsilon} \approx 10^{-3}$ /s) in the plastic range, using an MTS universal testing machine with a 250 kN load cell. Three specimens were tested for each condition

[1] Certain commercial instruments and software are identified to specify the experimental study adequately. This does not imply endorsement by NIST or that the instruments and software are the best available for the purpose.

to ensure repeatability of the results. Strain data were obtained using a 2D-Digital Image Correlation (2D-DIC) system (Correlated Solutions, Inc.) with a 5.0-megapixel camera (FLIR Grasshopper2) and 17 mm lens (Schneider). The specimens were prepared with a base coat of white paint with a black paint overspray pattern for the DIC imaging. The DIC parameters used in the analyses (VIC-2D software) were 19 pixels, 4 pixels, and 5 for the subset, step, and filter sizes, respectively. Figure 1 shows the experimental setup with the 2D-DIC system and specimen geometry from ASTM E8.

Figure *2* contains the true-stress strain curves during uniform elongation for seven uniaxial tension experiments (one for each orientation from the RD) and the corresponding instantaneous r-values, i.e., the ratio of width to thickness strain increment or $r = d\varepsilon_w^p / d\varepsilon_t^p$, with respect to equivalent plastic work. The instantaneous r-values are calculated using a constant plastic strain increment of 0.05. The thickness strain is inferred based on volume conservation. The equivalent plastic strain ( $\bar{\varepsilon} \equiv \int d\bar{\varepsilon}$ ), calculated by the work equivalence principle ($dw = \boldsymbol{\sigma}: \boldsymbol{d\varepsilon^p} = \bar{\sigma} \cdot d\bar{\varepsilon}$), is plotted in the upper x-axis. In Figure 2a, the RD and TD orientations show similar hardening behavior, and the true stress-strain curve for 45° falls slightly below the six other orientations as shown in the inset. Compared to the minor anisotropy in the flow stress seen in the stress-strain curves, the r-values present much clearer anisotropy, varying between 0.4 and 1.55, and even evolve as the plastic work increases. Young's modulus is calculated from the experimental data, and Poisson's ratio is assumed to be the textbook value. The values are summarized in Table 1.

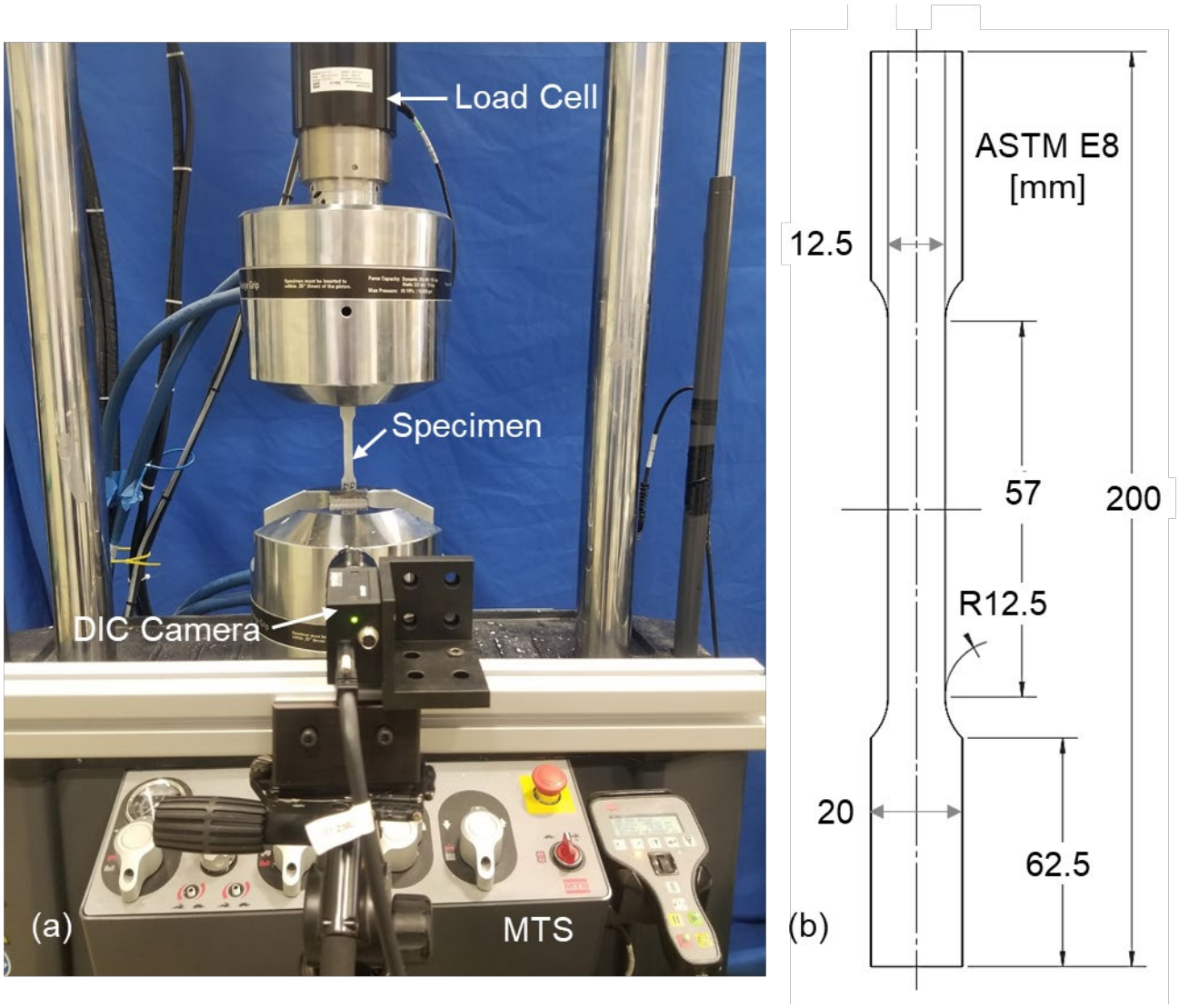


Figure 1. Uniaxial tension experiment: (a) test setup for MTS machine with 2D-DIC system and (b) ASTM E8 specimen geometry.

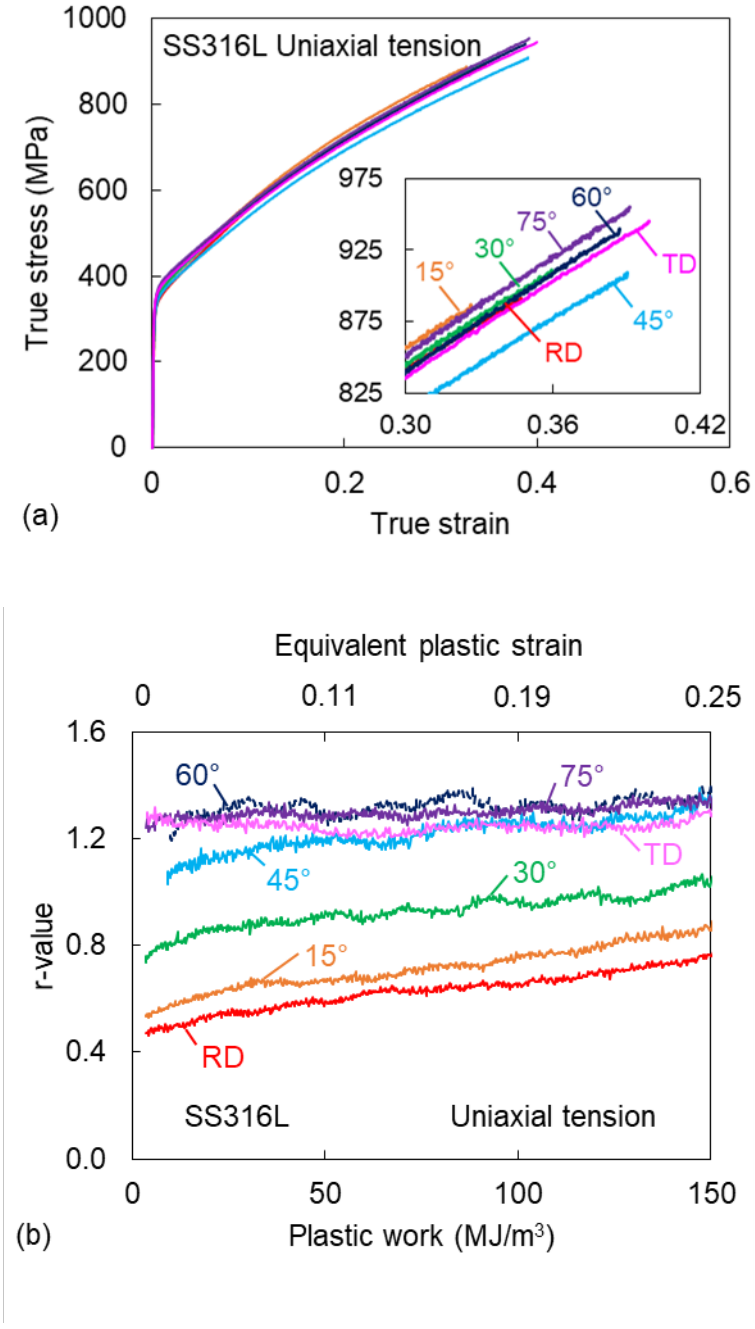


Figure 2. Experimental results of uniaxial tension in every 15° from the RD: (a) true stress-strain curves and (b) instantaneous r-values with respect to the plastic work and equivalent plastic strain.

## 2.2. Hydraulic bulge experiment

A hydraulic bulge experiment was performed using a servo-hydraulic formability tester (R&B RB316FT) with a 1000 kN (100 tonf) load cell and maximum hydraulic power unit flow rate of 0.757 L/s (12 gal/min) at the Korea Institute of Industrial Technology (KITECH). Square blanks of 200 mm x 200 mm size and 1.2 mm thickness were used with the holding force between 897 kN and 996 kN (90 tonf and 100 tonf). The strain field was measured using a stereo-DIC (surface 3D) system (GOM Inc.) with two 5.0-megapixel cameras (FLIR Grasshopper2) and 75 mm lenses (Schneider). The DIC analysis parameters used for the post-processing (ARAMIS Professional) were subset and step sizes of 19 pixels and 16 pixels, respectively. The experimental setup with the 3D-DIC system is shown in Figure 3.

According to ISO 16808 [52], in the bulge test, the stress-strain relationship is represented by the approximately equibiaxial, or membrane [76,77] stress and the thickness strain at the pole, which is determined by plastic incompressibility and the major and minor surface strains, i.e., $\varepsilon_1$ and $\varepsilon_2$, measured by the DIC system. The membrane stress, $\sigma_b$, is defined as $pR/(2t)$ where $p$ is the pressure recorded by the machine, $R$ is the radius of curvature of the outer surface, and $t$ is the thickness of the specimen. The instantaneous thickness is calculated by $t_0 \exp \varepsilon_t$, where $t_0$ is the initial sheet thickness and $\varepsilon_t$ is the true thickness strain determined by assuming incompressibility, i.e., $\varepsilon_t = -\varepsilon_1 - \varepsilon_2$. The radius of curvature of the outer surface is determined by $2/(\frac{1}{R_1} + \frac{1}{R_2})$, where $R_1$ and $R_2$ are the radii of major and minor curvatures of the outer surface at the pole obtained by the DIC system.

The experiment was performed five times to confirm test repeatability, and three of the results are shown in Figure 4a. The measured maximum strain for the bulge test, as commonly is seen, is higher than the maximum strain of uniaxial tension (also shown in Figure 4a), but the flow stresses are higher due to the plastic anisotropy and its evolution. This is characterized by normalizing the flow stress of equibiaxial tension with respect to the equivalent stress, which is uniaxial tension in the RD in this study, i.e., $\sigma_b/\bar{\sigma}$. The values at seven plastic work levels are summarized in Table 1. Similarly, the plastic anisotropy in strain is evaluated by the strain ratio in the RD and TD, i.e., $r_b = d\varepsilon_{TD}^p/d\varepsilon_{RD}^p$ [8], as shown in Figure 4b. Like in the plastic anisotropy observed in uniaxial tension, that of nearly equibiaxial tension also evolves during the deformation. It should be noted that the noise in the stress-strain curve causes an even greater noise level in the $r_b$ values of Figure 4b, but an evolution trend in the three experiments shown is captured. A previous study [78] found that the hydraulic bulge test does achieve a stress state that is perfectly equibiaxial tension. However, the amount of deviation reported is 1-5% for a steel material with an original thickness to diameter ratio between 0.01 and 0.001, which applies to the current work with a ratio of 0.004.

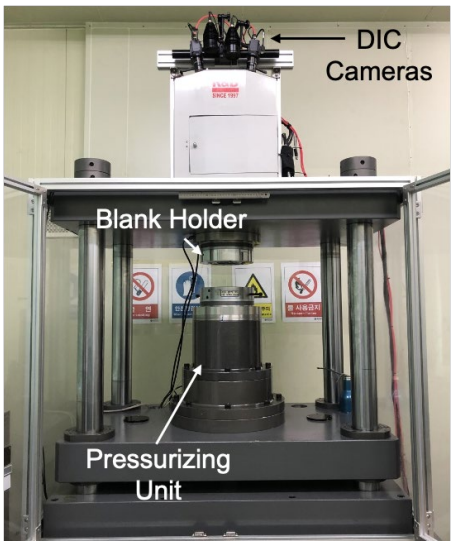


Figure 3. Hydraulic bulge test experimental setup (R&B RB316FT machine).

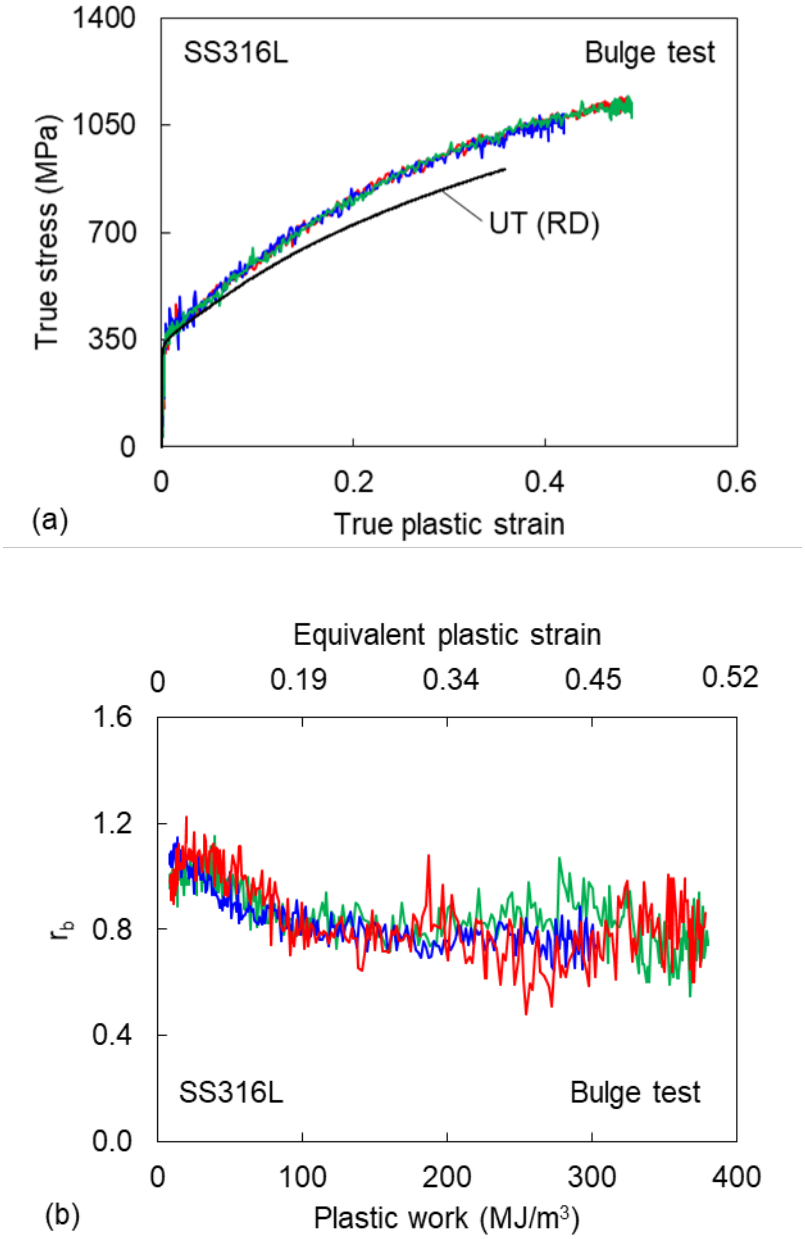


Figure 4. Experimental results of hydraulic bulge experiment: (a) true stress-strain curves of bulge test with comparison to uniaxial tension (UT) in the RD, and (b) $r_b$ value with respect to the plastic work and equivalent plastic strain.

Table 1. Summary of mechanical properties at seven plastic work levels for SS316L.

| Young's modulus | | $E = 193.8 \pm 0.4$ GPa | | | Poisson's ratio | | $\upsilon = 0.33$ | |
|---|---|---|---|---|---|---|---|---|
| Plastic anisotropy at seven plastic work levels $W^p$ | | | | | | | | |
| ($MJ/m^3$) | | 10 | 25 | 50 | 75 | 100 | 125 | 150 |
| Normalized stress ($\sigma/\bar{\sigma}$) | | | | | | | | |
| Uniaxial tension | RD | 1.000 | 1.000 | 1.000 | 1.000 | 1.000 | 1.000 | 1.000 |
| | 15 | 1.023 | 1.016 | 1.014 | 1.011 | 1.010 | 1.009 | 1.009 |
| | 30 | 1.024 | 1.008 | 1.001 | 1.001 | 1.000 | 0.998 | 0.998 |
| | 45 | 0.998 | 0.978 | 0.972 | 0.970 | 0.970 | 0.969 | 0.969 |
| | 60 | 1.041 | 1.010 | 0.995 | 0.994 | 0.993 | 0.992 | 0.992 |
| | 75 | 1.056 | 1.021 | 1.007 | 0.999 | 0.998 | 0.997 | 0.997 |
| | TD | 1.036 | 1.006 | 0.990 | 0.985 | 0.985 | 0.984 | 0.984 |
| Bulge | | 1.062 | 1.065 | 1.069 | 1.075 | 1.082 | 1.082 | 1.082 |
| Strain ratio (r-value and $r_b$) | | | | | | | | |
| Uniaxial tension | RD | 0.458 | 0.531 | 0.552 | 0.622 | 0.628 | 0.642 | 0.784 |
| | 15 | 0.564 | 0.604 | 0.696 | 0.696 | 0.746 | 0.821 | 0.839 |
| | 30 | 0.710 | 0.887 | 0.900 | 0.915 | 0.921 | 0.940 | 0.982 |
| | 45 | 1.004 | 1.124 | 1.156 | 1.180 | 1.203 | 1.262 | 1.279 |
| | 60 | 1.295 | 1.266 | 1.306 | 1.317 | 1.306 | 1.406 | 1.299 |
| | 75 | 1.322 | 1.276 | 1.355 | 1.306 | 1.333 | 1.341 | 1.421 |
| | TD | 1.335 | 1.315 | 1.313 | 1.261 | 1.227 | 1.242 | 1.252 |
| Bulge | | 0.969 | 0.940 | 0.900 | 0.872 | 0.865 | 0.865 | 0.865 |

*Determined normalized stresses typically had uncertainties ±0.003 and strain ratios typically had uncertainties ±0.0002 based on one standard deviation.

## 3. Constitutive modeling

In the following section, the modeling of the material behavior is discussed and is based on the experiments from the previous section. Yld2004-18p( $\bar{\varepsilon}$ ), a non-quadratic anisotropic yield function with equivalent plastic strain dependent parameters is used. Additionally, the Hockett-Sherby model is used to describe the strain hardening behavior.

### 3.1. Strain hardening

The strain hardening behavior is described by the Hockett-Sherby model [79]:

$$\bar{\sigma} = H - (H - \sigma_0) \cdot \exp(-N \cdot \bar{\varepsilon}^m) \quad (1)$$

where $\bar{\sigma}$ is the equivalent stress, $\bar{\varepsilon}$ is the equivalent plastic strain, and $\sigma_0$ is the initial yield stress measured using the 0.2% offset method. $H, N,$ and $m$ are material fitting parameters to the stress-strain curve of uniaxial tension in the RD as seen in Figure 5. One representative stress-strain curve of uniaxial tension in the RD is chosen for the fitting, and the identified values are summarized in Table 2.

Table 2. Material parameters for Hockett-Sherby strain hardening model.

| $\sigma_0$ (MPa) | $H$ (MPa) | $N$ | $m$ |
|---|---|---|---|
| 339.48 | 1445.44 | 1.81 | 0.89 |

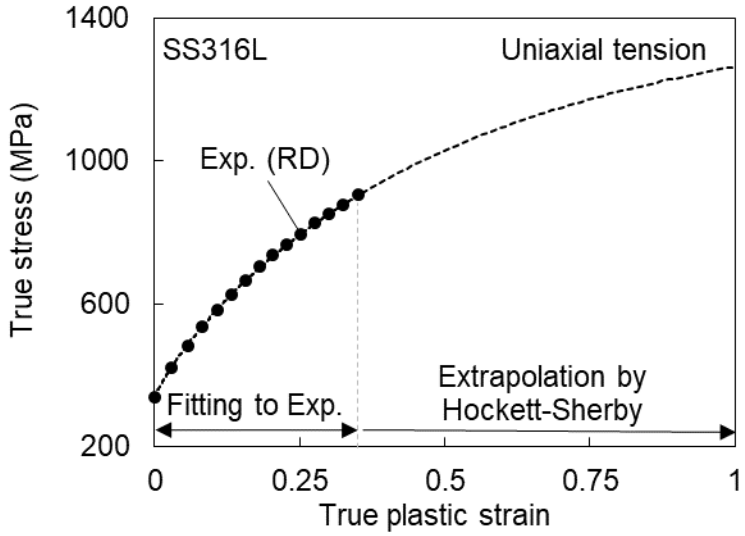


Figure 5. Extrapolation of stress-strain curve for uniaxial tension in the RD (symbols) using Hockett-Sherby model (dashed line).

To validate the extrapolation at larger levels of plastic strain, i.e., beyond the plastic strain range achieved by the uniaxial experiment, the stress-strain curve for Hockett-Sherby is also plotted for comparison with the equivalent stress-strain curve obtained from the bulge test experimental data using Hill 79 [80,81] (see Figure A1).

### 3.2. Yield function for plastic anisotropy and evolution

To model the plastic anisotropy and its evolutionary behavior with respect to plastic work, a non-quadratic anisotropic yield function, i.e., Yld2004-18p [9], is used:

$$\phi = \phi\left(\tilde{\mathbf{S}}', \tilde{\mathbf{S}}''\right) = \left|\tilde{S}_1' - \tilde{S}_1''\right|^a + \left|\tilde{S}_1' - \tilde{S}_2''\right|^a + \left|\tilde{S}_1' - \tilde{S}_3''\right|^a \tag{2}$$

$$+\left|\tilde{S}_2' - \tilde{S}_1''\right|^a + \left|\tilde{S}_2' - \tilde{S}_2''\right|^a + \left|\tilde{S}_2' - \tilde{S}_3''\right|^a$$
$$+\left|\tilde{S}_3' - \tilde{S}_1''\right|^a + \left|\tilde{S}_3' - \tilde{S}_2''\right|^a + \left|\tilde{S}_3' - \tilde{S}_3''\right|^a = 4\bar{\sigma}^a$$

where $\tilde{S}_i'$ and $\tilde{S}_j''$ are the principal values of the stress tensors, $\tilde{\mathbf{S}}'$ and $\tilde{\mathbf{S}}''$, which are linearly transformed deviatoric stresses by two operators, $\tilde{\mathbf{C}}'$ and $\tilde{\mathbf{C}}''$, respectively.

$$\begin{aligned}\tilde{\mathbf{S}}' &= \tilde{\mathbf{C}}' \cdot \mathbf{s} = \tilde{\mathbf{C}}' \cdot \mathbf{T} \cdot \boldsymbol{\sigma} = \tilde{\mathbf{L}}' \cdot \boldsymbol{\sigma} \\ \tilde{\mathbf{S}}'' &= \tilde{\mathbf{C}}'' \cdot \mathbf{s} = \tilde{\mathbf{C}}'' \cdot \mathbf{T} \cdot \boldsymbol{\sigma} = \tilde{\mathbf{L}}'' \cdot \boldsymbol{\sigma}\end{aligned} \tag{3}$$

where $\boldsymbol{\sigma}$ denotes the Cauchy stress tensor, $\mathbf{s}$ is its deviator, and $\mathbf{T}$ is the transformation tensor between them. The two transformation matrices, $\tilde{\mathbf{C}}'$ and $\tilde{\mathbf{C}}''$, are composed of eighteen parameters, i.e., $\alpha_{i=1-18} = \mathrm{c}_{12}', \mathrm{c}_{13}', \mathrm{c}_{21}', \mathrm{c}_{23}', \mathrm{c}_{31}', \mathrm{c}_{32}', \mathrm{c}_{44}', \mathrm{c}_{55}', \mathrm{c}_{66}', \mathrm{c}_{12}'', \mathrm{c}_{13}'', \mathrm{c}_{21}'', \mathrm{c}_{23}'', \mathrm{c}_{31}'', \mathrm{c}_{32}'', \mathrm{c}_{44}'', \mathrm{c}_{55}'', \mathrm{c}_{66}''$, where the subscripts denote the orientation with respect to the RD, given by:

$$\mathbf{C} = \begin{bmatrix} 0 & -c_{12} & -c_{13} & 0 & 0 & 0 \\ -c_{21} & 0 & -c_{23} & 0 & 0 & 0 \\ -c_{31} & -c_{32} & 0 & 0 & 0 & 0 \\ 0 & 0 & 0 & c_{44} & 0 & 0 \\ 0 & 0 & 0 & 0 & c_{55} & 0 \\ 0 & 0 & 0 & 0 & 0 & c_{66} \end{bmatrix} \tag{4}$$

$$\mathbf{T} = \frac{1}{3}\begin{bmatrix} 2 & -1 & -1 & 0 & 0 & 0 \\ -1 & 2 & -1 & 0 & 0 & 0 \\ -1 & -1 & 2 & 0 & 0 & 0 \\ 0 & 0 & 0 & 3 & 0 & 0 \\ 0 & 0 & 0 & 0 & 3 & 0 \\ 0 & 0 & 0 & 0 & 0 & 3 \end{bmatrix} \quad (5)$$

The exponent $a$ is related to the crystal structure, i.e., 6 for body-centered cubic (BCC) and 8 for face-centered cubic (FCC) [82,83]. The material used in the study is austenitic stainless steel (SS316L) with zero martensite in its as-received condition. Previous works by the authors [84,85] utilizing the same SS316L material confirm that the as-received material is fully austenitic and that minimal phase transformation occurs at room temperature. Thus, $a = 8$ is used for Yld2004-18p modeling in this study.

The plastic anisotropy, characterized by the strain ratios and normalized stresses from the uniaxial tension and hydraulic bulge experiments (Table 1), is used to determine the parameters of the yield function. For Yld2004-18p with constant parameters, the strain ratios and normalized stresses are averaged between plastic work levels of 10 and 150 MJ/m$^3$ to determine the constant parameter set (Table 3). For Yld2004-18p($\bar{\varepsilon}$), the individual sets of parameters at seven plastic work levels, i.e., $W^p$ from 10 to 150 MJ/m$^3$, equivalent to $\bar{\varepsilon}$ from 0.027 to 0.252, are determined separately, using the least squares method, to capture the evolution in the plastic anisotropy during the deformation. These are shown as the symbols in Figure 6.

Table 3. Summary of Yld2004-18p parameters:

| $\alpha_i$ | $A_i$ |
|---|---|
| 1 | 1.076 |
| 2 | 1.183 |
| 3 | 1.170 |
| 4 | 1.265 |
| 5 | 0.757 |
| 6 | 1.163 |
| 7 | 0.934 |
| 8 | 0.917 |
| 9 | 1.185 |
| 10 | 0.960 |
| 11 | 0.692 |
| 12 | 0.880 |
| 13 | 0.717 |
| 14 | 1.109 |
| 15 | 0.827 |
| 16 | 1.195 |
| 17 | 1.220 |
| 18 | 0.971 |

Next, each parameter, $\alpha_i$, is approximated using an exponential function with respect to the equivalent plastic strain, $\bar{\varepsilon}$, which is a simplified expression of Kuwabara et al. [25] as,

$$\alpha_{i,1-18}(\bar{\varepsilon}) = A_i - B_i \cdot \exp(-D_i \cdot \bar{\varepsilon}) \tag{6}$$

where $A_i, B_i$, and $D_i$ are calibration constants for each $\alpha_i$. The exponential fits are shown as lines with respect to plastic work and equivalent plastic strain in Figure 6. The corresponding calibration constants, i.e., the fitting parameters for each Yld2004-18p($\bar{\varepsilon}$) parameter, determined for SS316L are shown in Table 4.

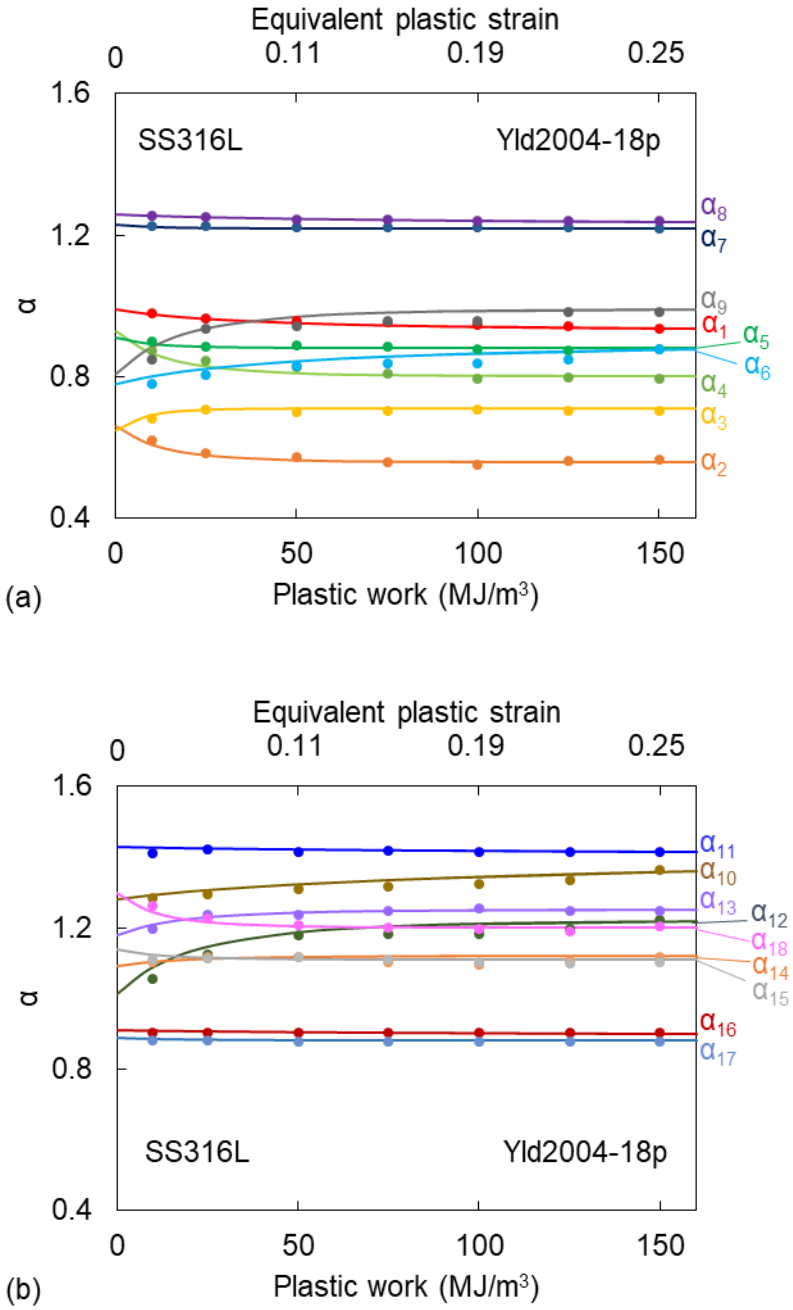


Figure 6. Equivalent plastic strain dependent parameters of Yld2004-18p($\bar{\varepsilon}$), i.e., $\alpha_i(\bar{\varepsilon})$ (a) $\alpha_1 - \alpha_9$ and (b) $\alpha_{10} - \alpha_{18}$, at seven levels of plastic work to capture the evolution of plastic anisotropy of SS316L. The parameters are fit (solid lines) with the exponential function in Equation 6 and the constants in Table 4.

Table 4. Summary of Yld2004-18p($\bar{\varepsilon}$) parameters: $\alpha_i(\bar{\varepsilon}) = A_i - B_i \cdot \exp(-D_i \cdot \bar{\varepsilon})$.

| $\alpha_i$ | $A_i$ | $B_i$ | $D_i$ |
|---|---|---|---|
| 1 | 0.93 | -0.06 | 10 |
| 2 | 0.56 | -0.10 | 27 |
| 3 | 0.71 | 0.06 | 45 |
| 4 | 0.80 | -0.13 | 25 |
| 5 | 0.88 | -0.03 | 35 |
| 6 | 0.89 | 0.11 | 8 |
| 7 | 1.22 | -0.01 | 30 |
| 8 | 1.23 | -0.03 | 5 |
| 9 | 0.99 | 0.18 | 20 |
| 10 | 1.40 | 0.12 | 4 |
| 11 | 1.40 | -0.03 | 3 |
| 12 | 1.22 | 0.21 | 17 |
| 13 | 1.25 | 0.07 | 20 |
| 14 | 1.12 | 0.03 | 20 |
| 15 | 1.11 | -0.03 | 27 |
| 16 | 0.89 | -0.02 | 3 |
| 17 | 0.88 | -0.01 | 20 |
| 18 | 1.20 | -0.10 | 30 |

*Determined $\alpha_i$ parameters typically had variances ±0.004 from identified values.

Figure 7 shows a comparison of the experimental (symbol) and predicted (dashed line) normalized stress and r-value of uniaxial tension from the RD to TD at seven plastic work levels. Stronger plastic anisotropy evolution is apparent in the r-value, i.e., the numerical values change significantly, e.g., from 0.458 to 0.784 in RD and from 1.004 to 1.279 at 45°, in the specified range, as the plastic work increases compared to the flow

stress in uniaxial tension. The calibrated parameters of Yld2004-18p($\bar{\varepsilon}$) capture the experiments reasonably well. During the calibration, a greater emphasis is placed on achieving better predictions at higher levels of plastic work, e.g., >50 MJ/m$^3$, than the lower levels, e.g., 10 MJ/m$^3$, assuming that the values saturate.

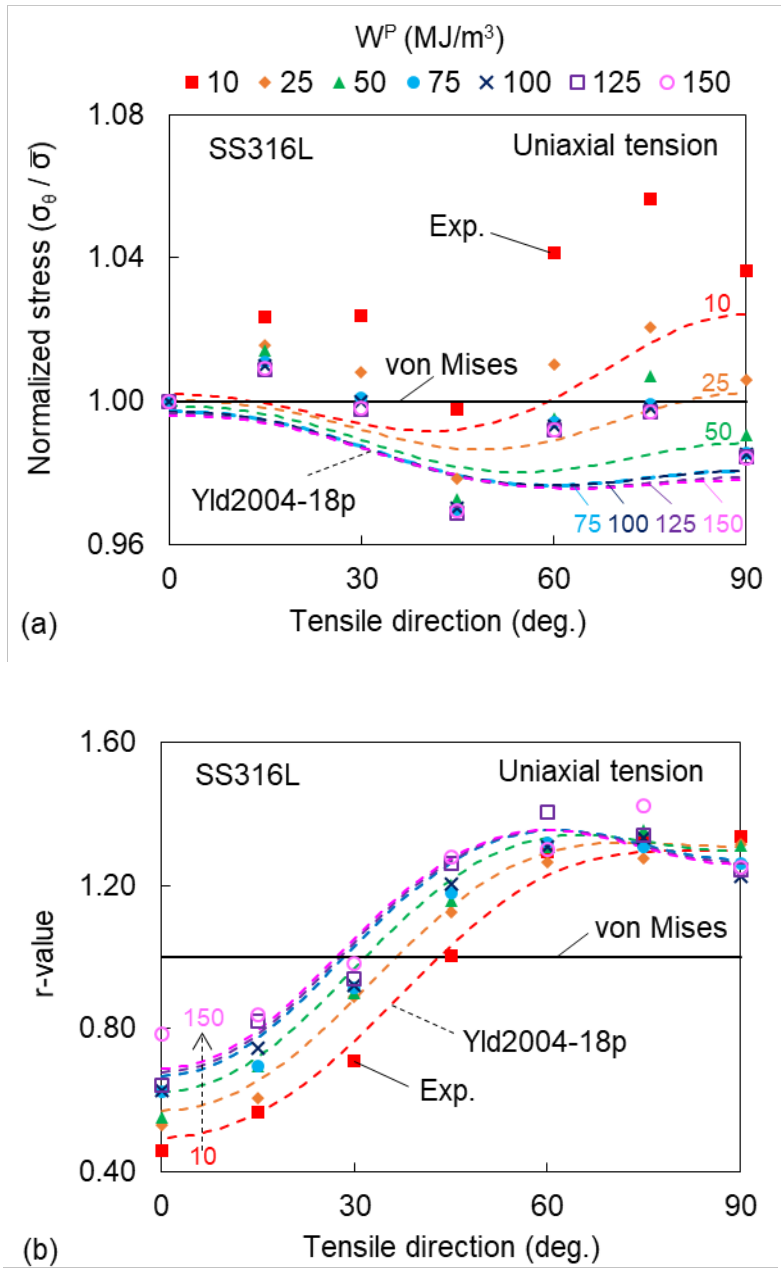


Figure 7. Parameter calibration of Yld2004-18p($\bar{\varepsilon}$) for uniaxial tension at seven plastic work levels (shown in legend symbols and colors): (a) normalized stress with respect to the flow stress of uniaxial tension in the RD and (b) r-value. Symbols denote the experiments, dashed lines denote Yld2004-18p($\bar{\varepsilon}$), and solid lines denote von Mises.

The yield locus evolution predicted by the determined material parameters is shown in Figure 8. Near the equibiaxial state, the yield locus is expanding as the plastic work increases, with a particularly significant increase between 10 MJ/m$^3$ and 25 MJ/m$^3$, as observable in the inset in Figure 8. Correspondingly, the yield locus appears to be contracting near the uniaxial tension in the TD state. The yield function, including the evolution of the $\alpha_i$ parameters, is implemented into a user material (UMAT) subroutine, for FE simulations using Abaqus/Standard 2019 [86]. The stress integration scheme used in the UMAT is the predictor-corrector method, proposed by Wilkins [87]. During the plastic correction, a semi-explicit method, i.e., General convex Cutting Plane Method (GCPM), proposed by Simo and Oritz [88], is used to update the stress states satisfying the consistency condition through iterations, projecting the stress onto the yield surface. GCPM is relatively simple to implement compared to a fully implicit method and still performs efficiently but requires careful time step control to guarantee numerical stability [89].

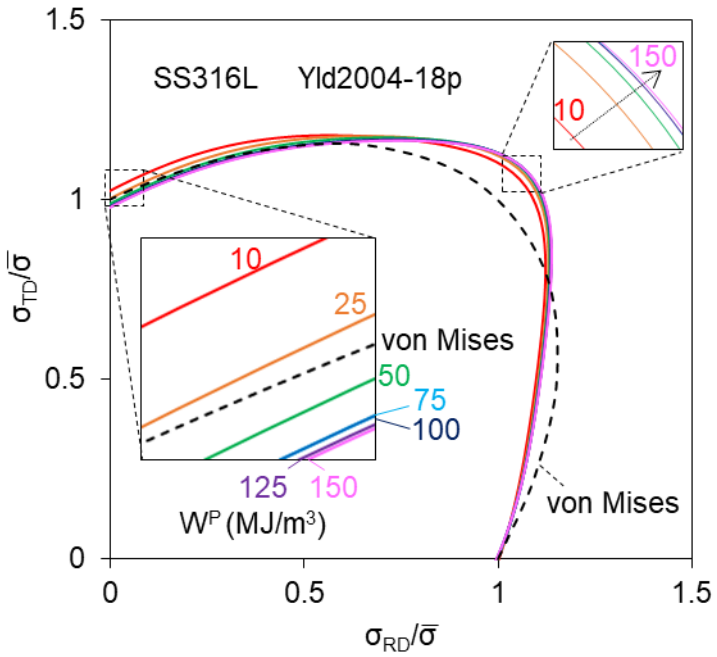


Figure 8. Evolution of Yld2004-18p($\bar{\varepsilon}$) yield locus at seven plastic work levels with insets highlighting shrinkage near plane strain and expansion near equibiaxial tension.

## 4. In-plane biaxial tension using cruciform specimen

Cruciform biaxial experiments using a custom designed cruciform specimen were performed to validate the ability of the implemented plasticity models, i.e., Yld2004-18p($\bar{\varepsilon}$) combined with the Hockett-Sherby model, to capture the plastic anisotropy evolution during the in-plane biaxial deformation. This section describes the optimization of a cruciform geometry based on six design goals and the experiments using the determined specimen under four proportional loading conditions.

### 4.1. Design of customized cruciform specimen

A design of experiments (DOE) approach was taken to generate a cruciform geometry suitable for the biaxial machine at the University of New Hampshire (UNH). The

previous iteration of this geometry is found in [65], which was a scaled version of the geometry developed in [44]. The design goals in this work were (1) maximized strains in the gauge section, (2) nearly linear strain paths, (3) moderate strain uniformity in the gauge area, i.e., ±2.5 % of the mean strain value, (4) sufficient gauge area for material characterization, e.g., DIC, magnetic induction, and microstructure image scans, (5) a machinable final geometry, and (6) a suitable design for the UNH apparatus, e.g., grip widths, force capacity, displacement, and thickness.

The key geometric features for the design (as shown in Figure 9) were the radius of the pocket flat area ($R_{gauge}$), fillet in the pocket ($F_{pocket}$), thickness of the flat area within the pocket ($T_{pocket}$), corner notch radius ($R_{notch}$), and arm width ($W_{arm}$). It should be noted that $T_{pocket}$ was set to 0.6 mm, corresponding to a 50 % thickness reduction, since this parameter will always trend to the smallest value allowed in the design space to achieve the design goals, especially maximizing strain in the gauge area. The lower and upper bound values of $R_{gauge}$ were selected to allow sufficient surface area for measurement, e.g., DIC, magnetic induction, etc. The lower bound of $F_{pocket}$ was set to 0.25 mm, which is approximated as the machinability limit of standard end mills. Geometric requirements dictate that the minimum $W_{arm}$ is a function of $F_{pocket}$ and $R_{gauge}$ (see Appendix A.2). Further based on literature and prior experience, $R_{notch}$ was selected to be $W_{arm}/6$. $R_{pocket}$ is the radius of the pocket, as depicted in Figure 9, and is geometrically derived from $F_{pocket}$ and $R_{gauge}$ (see Appendix A.2). The overall width of the specimen $W_{specimen}$ was set to 180 mm to allow for sufficient gripping in the UNH biaxial machine. The constraints on the design parameters are shown in Table 5.

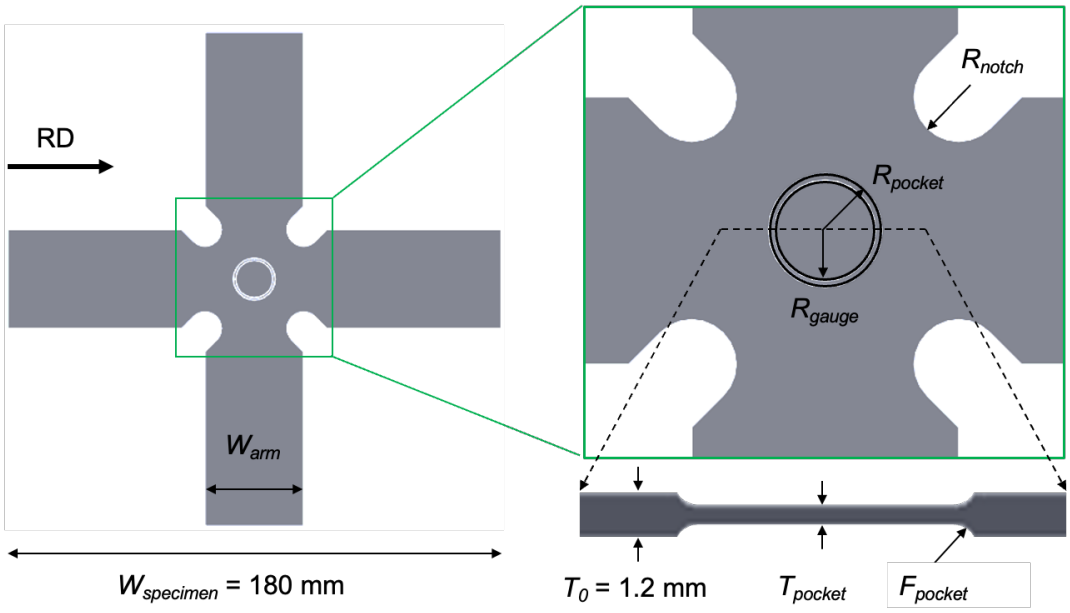


Figure 9. Novel cruciform specimen geometry with a reduced thickness pocket area and corner notch features in variable terms.

Table 5. Lower bound, upper bound, and optimized values for key design parameters.

| Design parameter (mm) | Lower bound | Upper bound | Optimized |
|---|---|---|---|
| Radius of pocket flat area ($R_{gauge}$) | 4 | 15 | 5.65 |
| Fillet in pocket ($F_{pocket}$) | 0.25 | 4 | 1.50 |
| Arm width ($W_{arm}$) | 6.50 | 30 | 30 |
| Thickness of pocket ($T_{pocket}$) | 0.6 | | 0.6 |
| Corner notch radius ($R_{notch}$) | $W_{arm}/6$ | | 5 |

For the specimen optimization, a two-level DOE approach was implemented in a commercial optimization software, Isight [90], which is a plug-in for Abaqus, as seen in Figure 10. Orange “process component” and green “application component” boxes, per

Isight nomenclature, are noted in the figure. In the first level DOE, DOE1 module, 32 unique pairs of $F_{pocket}$ and $R_{gauge}$ were selected within the limits listed in Table 5 using the Optimum Latin Hypercube method. Then, the $W_{logic}$ Calculation module determined the minimum values of $W_{arm}$ based on the equations in Appendix A.2 and passed them to the next level. In the second level DOE, DOE2 module, 32 unique values of $W_{arm}$ were identified again using the Optimum Latin Hypercube method. Through the DOE1 and DOE2 modules, 32 x 32 (1024) combinations of the three design parameters ($F_{pocket}$, $R_{gauge}$, and $W_{arm}$) were produced. For each of the 1024 combinations in turn, the $R_{notch}$ Calculation module determined $R_{notch}$. Then, the variables for each of the 1024 combinations were used in the parameterized FE model (presented in detail in Section 5), and the analysis was run with the same displacement boundary conditions as the experiments. Isotropic hardening and von Mises yield function were assumed in the DOE FE simulations to reduce the computation time.

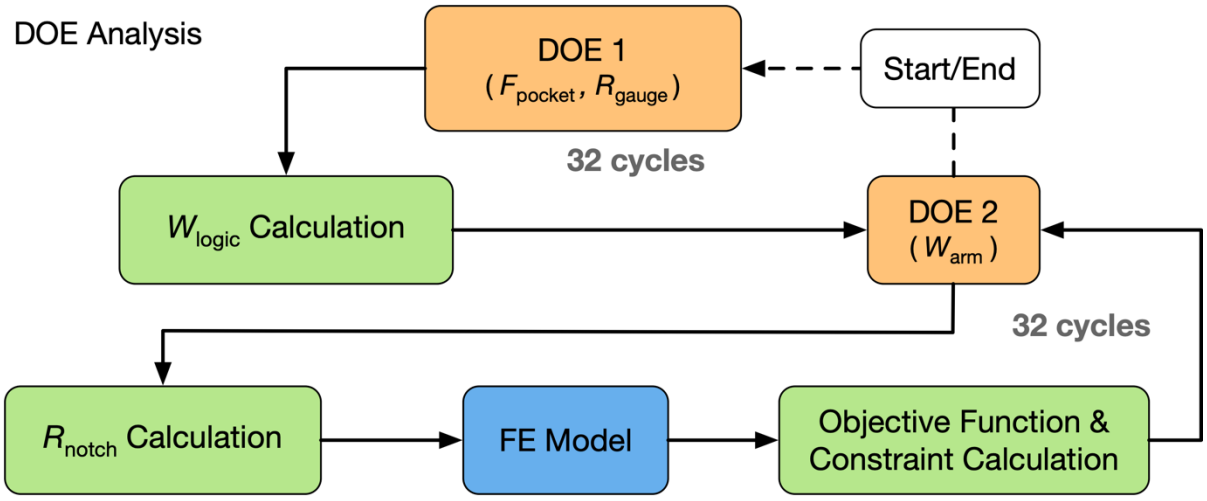

Figure 10. Schematic of process flow in DOE study for cruciform specimen geometry with orange “process component”, green “Java application component”, and blue "FE model application component" boxes per Isight nomenclature noted.

Each run was assessed in the Objective Function & Constraint Calculation module using an objective function and constraint selected to maximize the average effective strain in the center 3 mm radius of the pocket. This is assumed to be a sufficient area for material characterization instruments within $R_{gauge}$, provided that the required uniformity of equivalent plastic strain is also achieved. These are formulated as,

$$\overline{(\bar{\varepsilon})}_{R\leq 3} = \frac{1}{n}\sum_{i=1}^{n}\left[\bar{\varepsilon}\left(\sqrt{x_i^2 + y_i^2} \leq 3\right)\right]$$
$$\text{Maximize}\left[\overline{(\bar{\varepsilon})}_{R\leq 3}\right] \tag{7}$$

with a constraint of ±2.5 % variation,

$$\text{While}\left[0.975\overline{(\bar{\varepsilon})}_{R\leq 3} \leq \left(\bar{\varepsilon}\left(\sqrt{x_i^2 + y_i^2} \leq 3\right)\right) \leq 1.025\overline{(\bar{\varepsilon})}_{R\leq 3}\right] \tag{8}$$

where, $\bar{\varepsilon}$ is the equivalent plastic strain, $x_i$ and $y_i$ are the x and y coordinates, respectively, of the nodes in the undeformed configuration, and $R$ is the radius from the central point of the pocket. The value of the objective function was then passed to the DOE2 module and evaluated for the constraint conditions. This process continued for all

1024 FE analyses. To ensure the applicability of the optimized design to different deformation modes, the DOE process was performed separately for three boundary conditions, i.e., $\delta_x$: $\delta_y$= 1:1, 2:1, and 4:1 covering from equibiaxial to plane-strain, where $\delta_x$ and $\delta_y$ are displacements in each direction. The final dimensions for the geometric parameters are shown in Table 5.

### 4.2. In-plane biaxial tension experiment

The in-plane biaxial tension experiments were performed using the cruciform specimen optimized in Section 4.1. The cruciform specimens were fabricated at UNH by the following steps. First, the specimen outline of the cruciform shape was waterjet cut from as-received 1.2 mm thick ($T_0$) SS316L sheets. The perimeters were then lightly sanded to remove any rough edges. Next, the pockets on both sides of the specimen were milled to reduce the thickness, using a custom fixture to prevent bending during the milling operation, and finally polished to reduce the surface roughness using a series of diamond pastes in conjunction with wool bobs attached to a rotary tool.

The in-plane biaxial tension experiments were conducted using a custom loading frame at UNH, that is described in [59,91,92] and shown in Figure 11. The 3D-printed alignment fixture was utilized to center the specimens prior to gripping, and the pantograph ensured that the motion along each axis was symmetrical about the center. The biaxial machine recorded voltages corresponding to force and displacement values during experiments in synchronization with the stereo-DIC (3D surface DIC from Correlated Solutions, Inc.). The strain data were extracted in the center of the pocket in

the post-processing software (VIC-3D) with the following parameters: 21 pixels, 5 pixels, and 5 for the subset, step, and filter sizes, respectively.

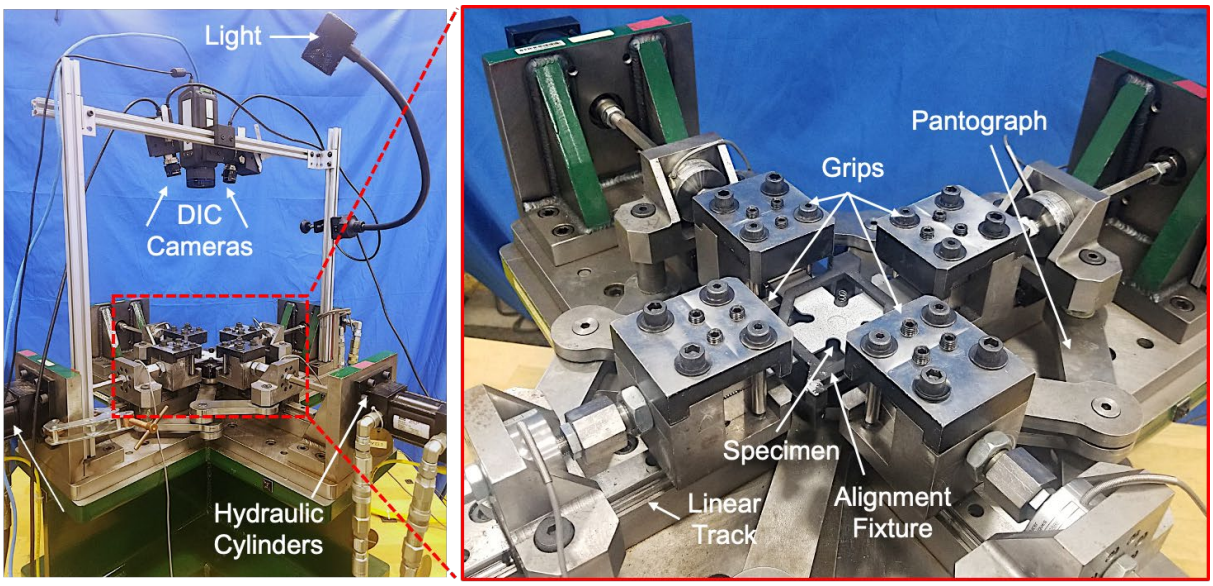


Figure 11. In-plane biaxial tension experimental setup (custom machine at UNH).

The specimens were subjected to four loading conditions, programmed as the displacement paths in x- and y-axis (aligned with the material orientation, RD and TD, respectively), i.e., $\delta_x$:$\delta_y$ = 1:1, 2:1, 8:1, and 1:free (unconstrained in y-axis), by driving the four hydraulic cylinders. The experimental displacement paths are shown in Figure 12. The order of displacement ratios $\delta_x$:$\delta_y$=1:1, 2:1, 8:1, 1:free result in deformation close to equibiaxial, through plane strain, to a near uniaxial strain path in the gauge section. The corresponding experimental results are given in Section 5 with the simulation results.

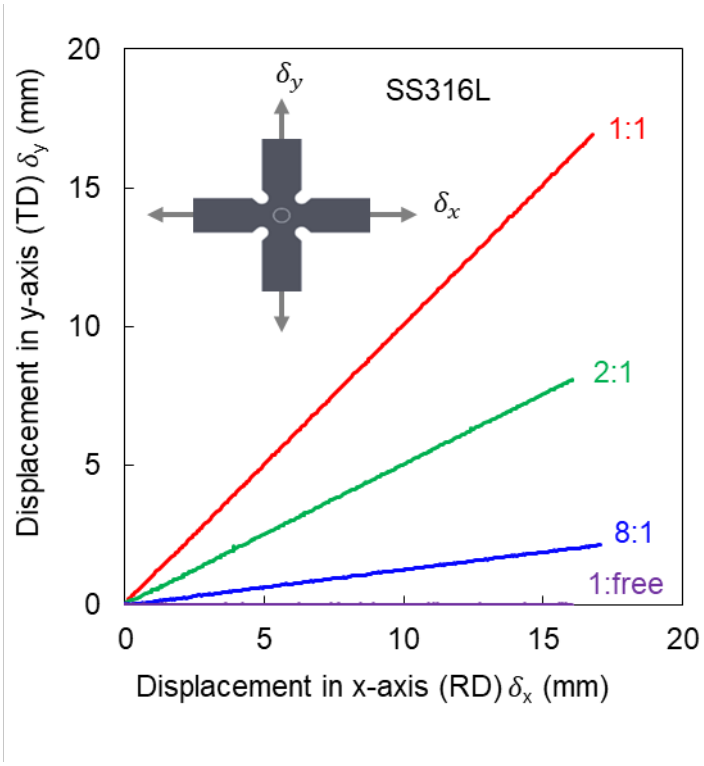


Figure 12. Biaxial tension experimental displacement paths along x-axis (RD) and y-axis (TD).

## 5. FE simulation for in-plane biaxial tension

To validate the material model from the previous section, finite element simulations are detailed in the following section. A summary of the finite element model is given. Comparisons of the anisotropic plasticity model with experiments and von Mises are also presented.

### 5.1. FE model details

An FE model of the cruciform specimen for in-plane biaxial tension was created in Abaqus/Standard 2019. A one-eighth model was used, due to three planes of symmetry, with a shortened arm length in comparison to the physical specimens, i.e., 65 mm

specimen half-length instead of 90 mm, to exclude the clamped portion of the specimen arm. The model was meshed using linear brick elements with reduced integration (C3D8R) and consisted of approximately 22,000 elements in total, with finer meshing in the center pocket region and three elements through the half-thickness as shown in Figure 13. Note that a coarser mesh was used for the optimization described in Section 4.1 to reduce the computational expense.

The plasticity models implemented as a UMAT subroutine in Abaqus/Standard 2019 were used for the FE simulations, which include a non-quadratic anisotropic yield function with the equivalent plastic strain dependent parameters, i.e., Yld2004-18p($\bar{\varepsilon}$), to capture the plastic anisotropy evolution and Hockett-Sherby model to describe the strain hardening behavior, as explained in Section 3. A quadratic isotropic yield function, i.e., von Mises, combined with the same strain hardening description, is compared with the implemented plasticity models.

The displacement boundary conditions were applied to two reference points, which were kinematically coupled to the thickness surfaces at the end of the specimen arms in the x- and y-axis. Force and displacement data were extracted from these reference points, and strain data was extracted from the center of the pocket surface as marked in Figure 13 (red dot labeled $\varepsilon$ in the through-thickness section insert).

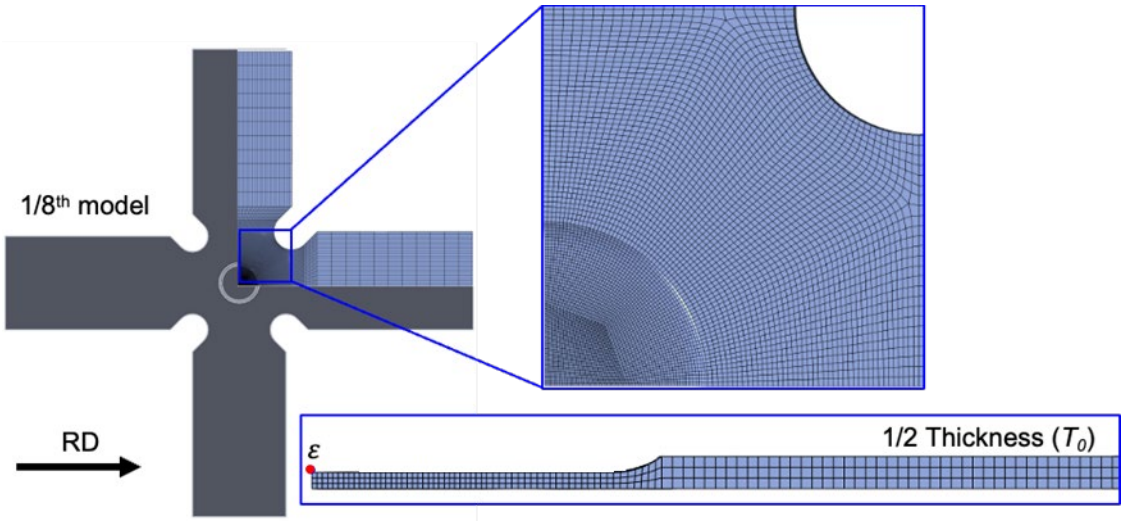


Figure 13. 1/8th symmetry cruciform FE model and mesh design with C3D8R elements (not to scale).

### 5.2. Anisotropic plasticity model validation

The force-displacement curves extracted from the experiments and simulations are compared in Figure 14. For consistency in Figure 14 and all subsequent figures, the simulation curves are truncated at the maximum displacement achieved by the experiments, i.e., the fracture displacement. Note that the von Mises prediction for the $\delta_x$: $\delta_y$ =1:1 loading condition is an exception and is truncated at a slightly smaller displacement than the experiments due to early localization predicted in the simulation.

Under all four loading conditions, Yld2004-18p($\bar{\varepsilon}$) predicts the experimental force-displacement curves well while von Mises overpredicts the force value for nearly the entire displacement range. This is likely due to the quadratic feature and isotropic nature of the von Mises model, which are demonstrated in the material characterization in Section 2. Yld2004-18p tends to overpredict or underpredict the force value for the four cases shown. Considering that complicated, non-uniform deformation fields can be

developed in this cruciform specimen, the accuracy of the material description for a wide range of plastic deformation modes can affect the prediction.

Furthermore, the local strain paths extracted from the surface at the center of the pocket (red dot in Figure 13), were compared for four loading conditions as shown in Figure 15. Only local strains in the RD ($\varepsilon_{RD}$) and TD ($\varepsilon_{TD}$), i.e., x- and y-axis, respectively, were considered in the strain path plot. The symbols in Figure 15 represent the experimental data from the same location and show the higher maximum achievable strain using the customized cruciform specimen compared to specimens used in past research [59]. The result indicates that the considered specimen design goals, i.e., (1) greater deformation compared to the standard specimen and (2) linear strain paths, are successfully achieved in the experiment.

Overall, in Figure 15, the strain predictions by Yld2004-18p($\bar{\varepsilon}$), Yld2004-18p, and von Mises models agree reasonably well with the experiments. Still, Yld2004-18p($\bar{\varepsilon}$) captures the strain paths, especially near plane strain given by $\delta_x$: $\delta_y$= 8:1 and 2:1, more accurately than von Mises. The final strain levels, i.e., the end point in the curves shown in Figure 15, selected at the same final displacements as experiments, are also consistently overpredicted by von Mises. This seems to be caused by the isotropic assumption ignoring the plastic anisotropy developed by complicated, non-uniform plastic deformations in the surrounding area as shown in Figure 16. Comparing Yld2004-18p and Yld2004-18p($\bar{\varepsilon}$), Yld2004-18p($\bar{\varepsilon}$) shows better agreement with the experimental data.

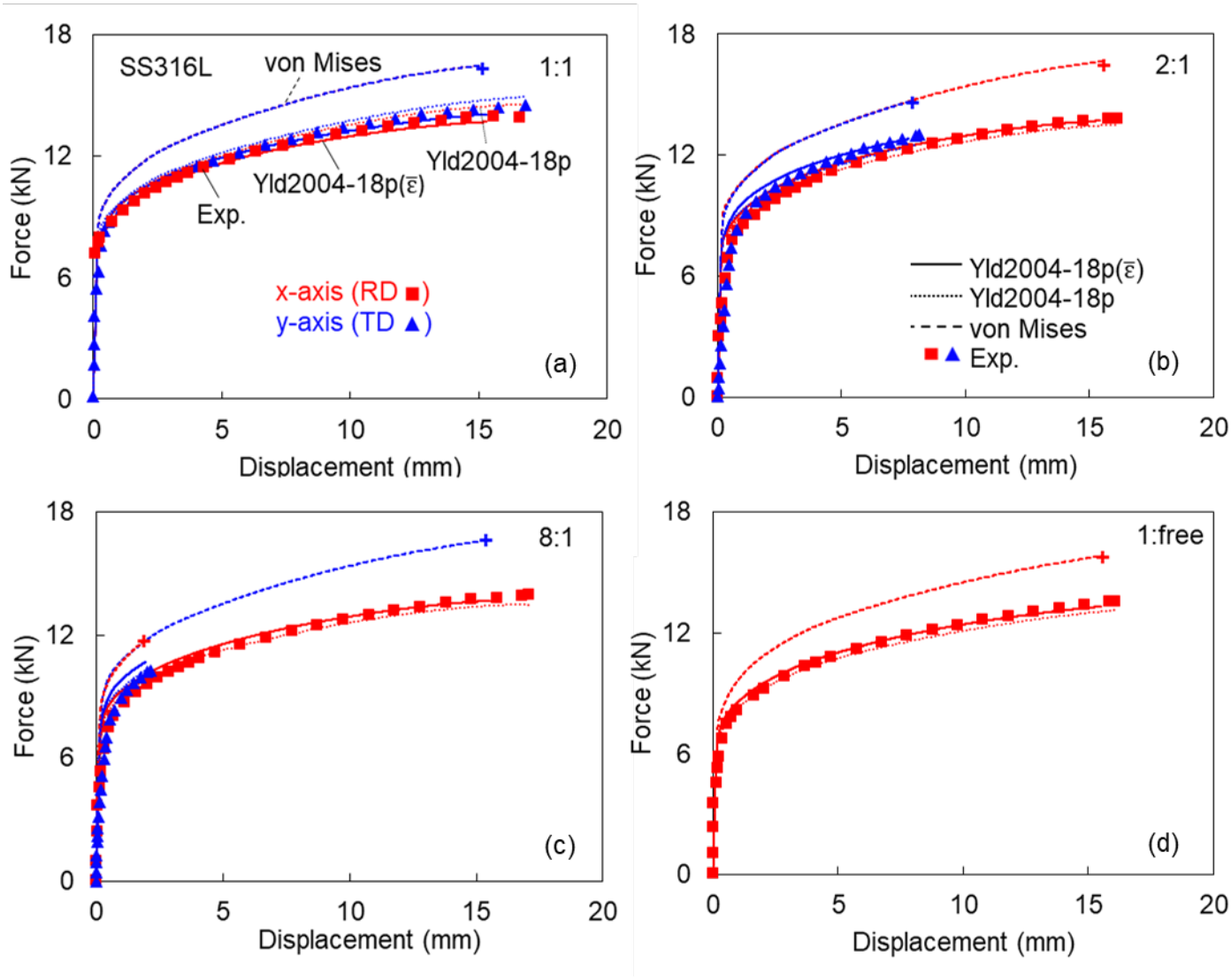


Figure 14. Force-displacement curves comparing Yld2004-18p($\bar{\varepsilon}$) (solid lines), Yld2004-18p (dotted lines), von Mises (dashed lines with end points denoted by plus signs), and experimental (square and triangle symbols) results for proportional loading paths: $\delta_x$: $\delta_y$= (a) 1:1, (b) 2:1, (c) 8:1, and (d) 1:free. RD and TD are aligned along the x-axis (red) and y-axis (blue), respectively.

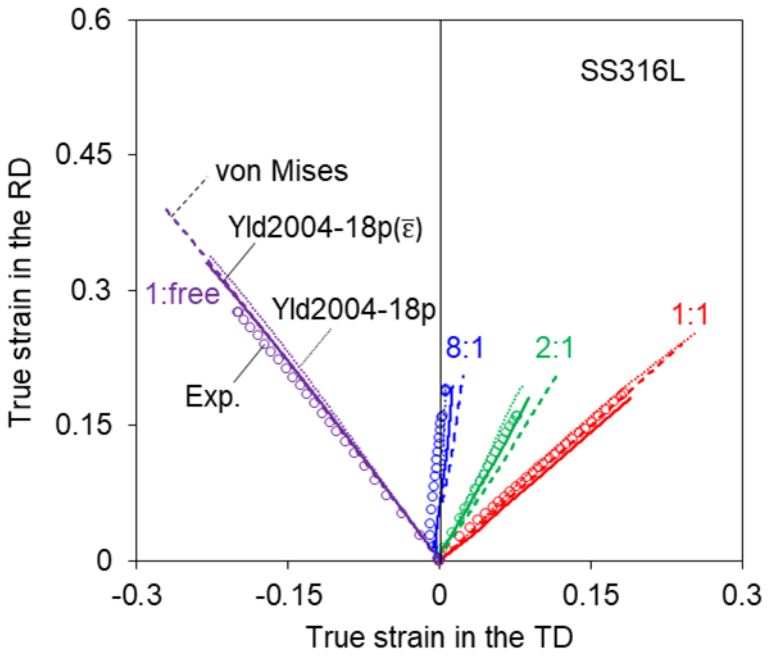


Figure 15. Strain path comparison between Yld2004-18p($\bar{\varepsilon}$) (solid lines), Yld2004-18p (dotted lines), von Mises (dashed lines), and experimental (symbols) results for $\delta_x$: $\delta_y$=1:1, 2:1, 8:1, and 1:free.

Figure 16 shows close-ups of the strain fields in the pocket and the surrounding area, including the notches, just prior to fracture and at the same instance as the force-displacement (Figure 14) and strain paths (Figure 15) for the simulations. Commonly in all loading conditions, the highest maximum principal strain is observed near the notches, which eventually leads to fracture in the specimen. As observed in the comparison of the strain paths, the predictions of the strain contours in the pocket region from Yld2004-18p($\bar{\varepsilon}$) show better agreement with experiments than those of Yld2004-18p and von Mises. The predictions of Yld2004-18p match the experimental strain contours better than the predictions of von Mises, but both are unable to capture some of the subtle strain

gradients evident in the DIC experimental images, e.g., the minimum principal strain variation in the radial direction in the specimen pocket for the $\delta_x$: $\delta_y$= 1:1 and 1:free experiments.

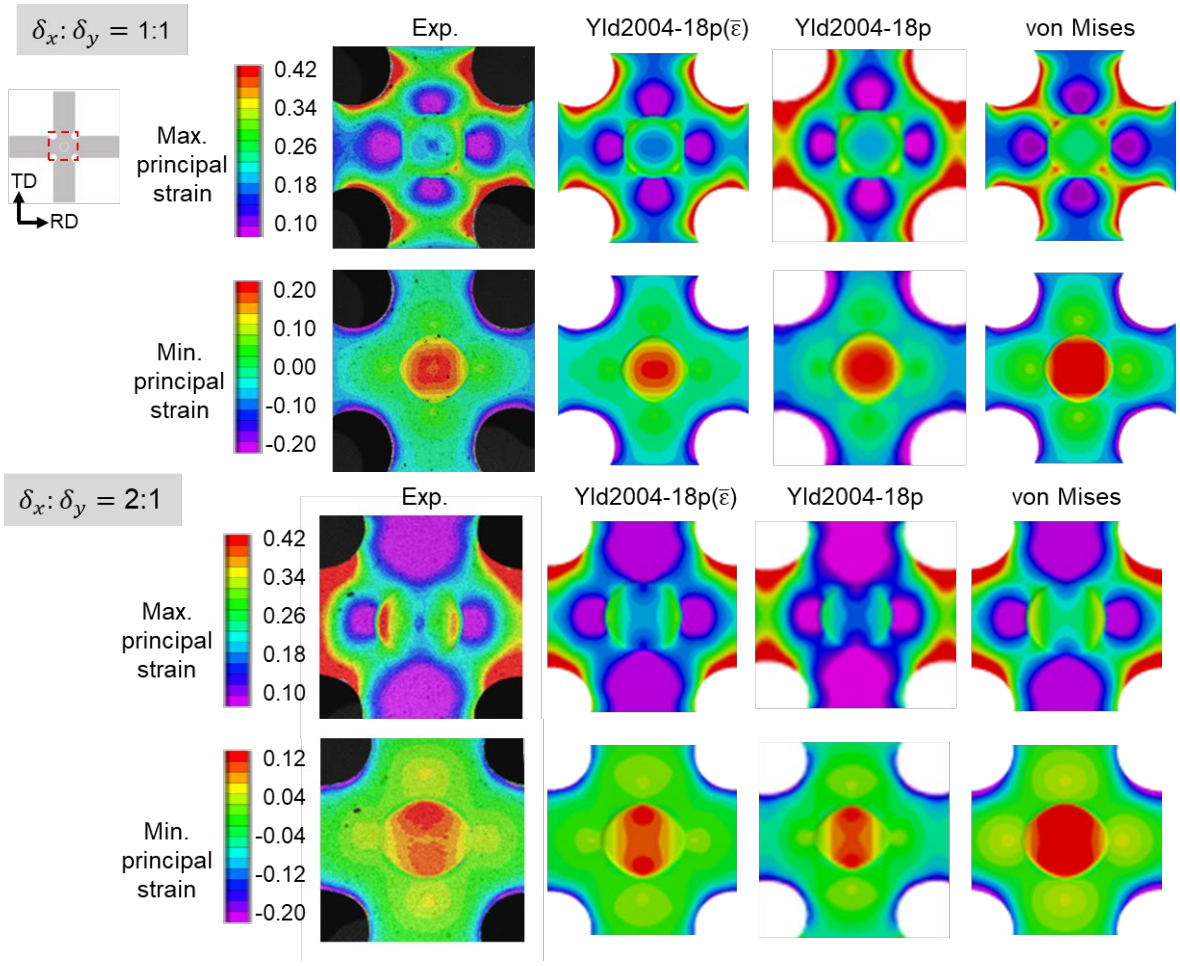

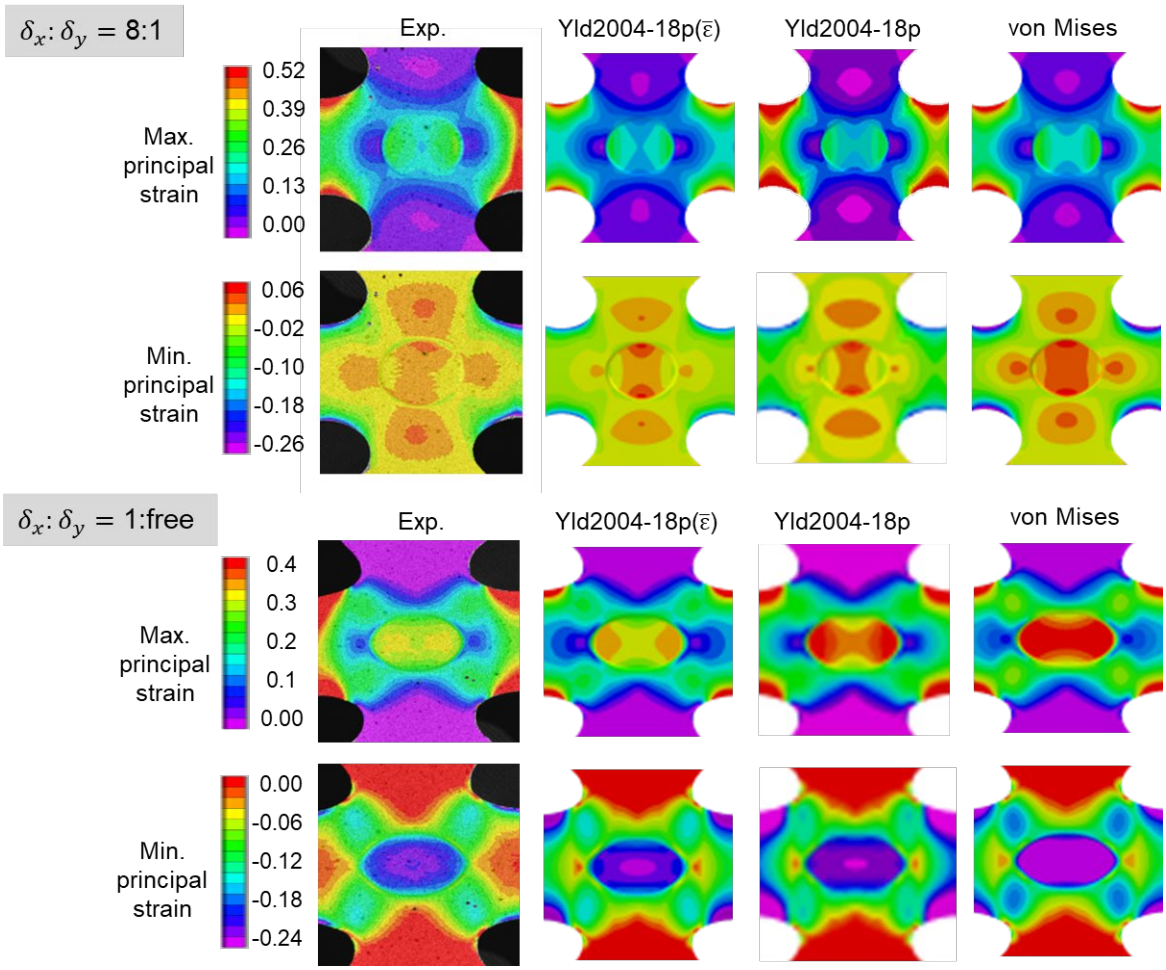


Figure 16. Comparison of principal strain contours captured at the same fracture displacement as the experiment to Yld2004-18p( $\bar{\varepsilon}$ ) and von Mises models with proportional loading: $\delta_x$: $\delta_y$= (a) 1:1, (b) 2:1, (c) 8:1, and (d) 1:free.

To evaluate the deformation uniformity in the gauge area, the equivalent stress and strain in the thickness (RD-ND plane) and the face (RD-TD plane) of the pocket are examined based on the numerical predictions (see Figure 17). Note that, for simplicity, the predictions of Yld2004-18p are not shown in Figure 17. In the reduced thickness region, the stress and strain are nearly constant through the specimen thickness and along the radial direction on the face. Overall, these predictions indicate that relatively

uniform fields for the equivalent stress and strain are achieved over a large volume, which is desirable for material characterization measurements, e.g., DIC, magnetic induction.

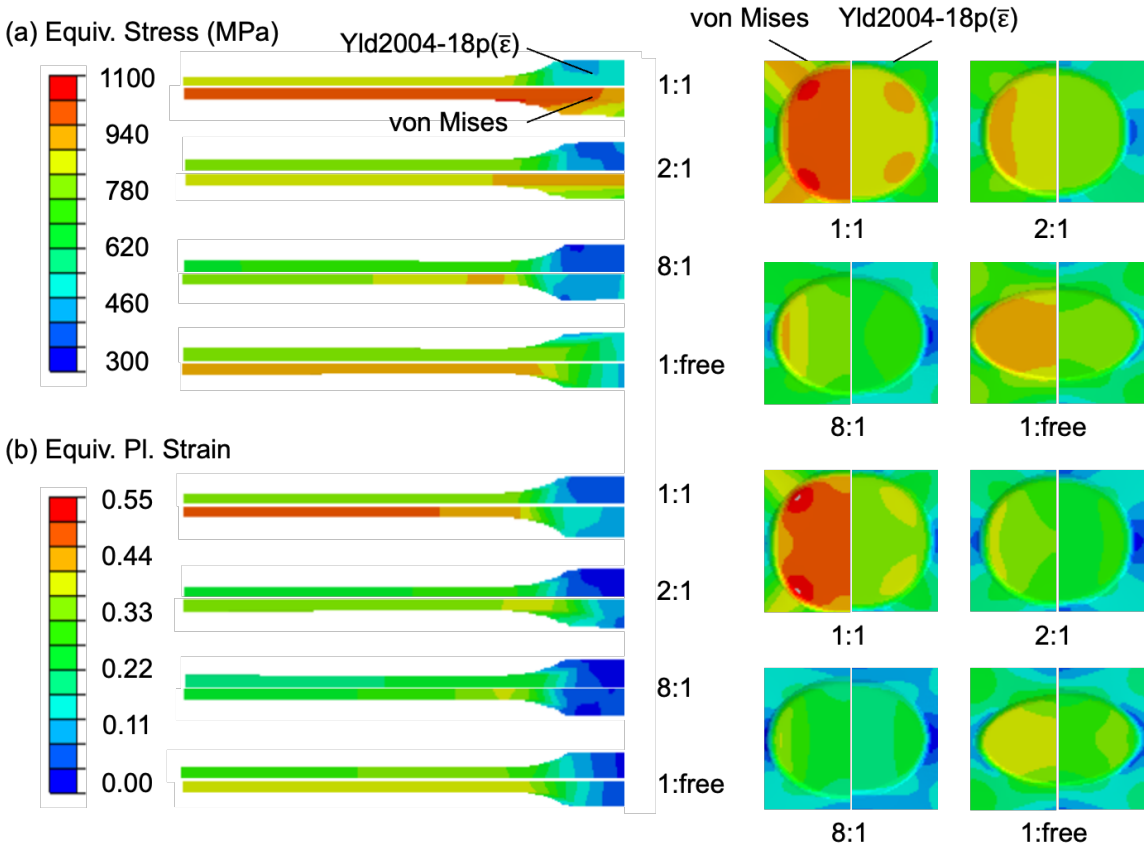


Figure 17. Comparison of equivalent (a) stress and (b) plastic strain along the thickness direction (RD-ND plane) and the face (RD-TD plane) of the pocket.

## 6. Summary and conclusions

In this work, the plastic anisotropy of SS316L and its evolutionary behavior were investigated under proportional loading paths using a cruciform specimen customized for in-plane biaxial experiments. The plastic behavior, characterized by uniaxial and equibiaxial tension experiments, were modeled by a non-quadratic anisotropic yield

function with equivalent plastic strain dependent material parameters, Yld2004-18p($\bar{\varepsilon}$), to capture the strong evolutionary behavior in the plastic anisotropy and Hockett-Sherby model to describe the strain hardening. For the in-plane biaxial tension, a cruciform specimen was newly designed to satisfy six design goals and improve the specimen performance in experiments. Four loading paths were applied to the specimen, imposing strain paths near uniaxial, plane-strain, and equibiaxial tension. The experiments were performed using the in-plane biaxial machine at UNH, and the results were compared with FE simulations using the implemented models in a UMAT for Abaqus/Standard. Overall, the Yld2004-18p($\bar{\varepsilon}$) predictions show good agreement with the experimental results for both the force-displacement curves and the strain fields in the gauge region compared to the constant parameter and isotropic yield functions. This validates that the implemented plasticity modeling can accurately describe the plastic anisotropy developed in both stress and strain fields.

**Acknowledgements**

This work is partially funded by the NH BioMade Project, which is supported by the US National Science Foundation EPSCoR award (NSF #1757371). The authors would like to thank Matthew Eaton and Jordan Hoffman for their contributions to the FE simulations, Scott Campbell in the UNH College of Engineering and Physical Sciences Machine Shop for his assistance with specimen fabrication and fixture design, Marguerite Kennish and Mohammad Ali Davarpanah for their assistance with the uniaxial experiments, and Dr. Yumi Choi from Seoul National University for conducting the bulge test experiments at KITECH.

## Appendix
## A.1. Comparison of Effective Stress-Strain Curves for Bulge Test

A comparison of the strain hardening behavior at large, i.e., close to 1, strain levels is shown in Figure A1 to further validate the chosen material model. To simplify the calculations, instead of using Yld2004-18p, the bulge test equivalent stress-strain curve is obtained by the Hill 1979 non-quadratic yield function (Equation 1.1) [80]. The equations for the equivalent stresses and strains for a balanced biaxial stress state [81] are given in Equation A1.2, where $\varepsilon_1$ is half of the absolute value of the thickness strain, $a$ is calculated by equating the equivalent stress and strain from a tensile test and bulge test at an effective strain equivalent to the true uniform strain in tension, and $r_2$ is the r-value obtained by $r = (r_0 + 2r_{45} + r_{90})/4$. The Hill 1979 effective stress-strain curve for the bulge test (red circles) is plotted with the extrapolated Hockett-Sherby stress-strain curve. Overall, the Hill 1979 stress-strain curve matches well with the Hockett-Sherby stress-strain curve over the entire strain range shown.

$$2(1 + r_2)\bar{\sigma}^a = (1 + 2r_2)|\sigma_1 - \sigma_2|^a + |\sigma_1 + \sigma_2|^a \tag{A1.1}$$

$$\bar{\sigma} = \frac{2\sigma_1}{[2(1 + r_2)]^{1/a}} \quad ; \quad \bar{\varepsilon} = \varepsilon_1[2(1 + r_2)]^{1/a} \tag{A1.2}$$

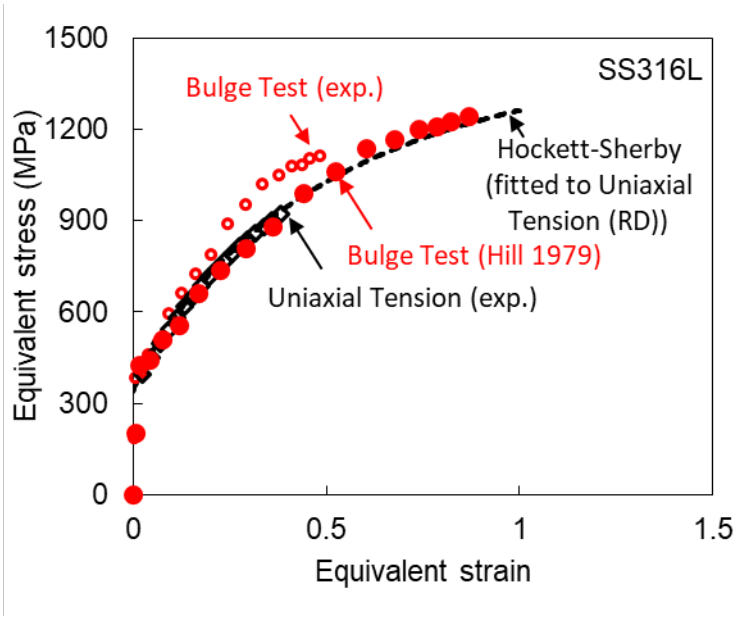


Figure A1. Comparison of extrapolated Hockett-Sherby (black dashed line) stress-strain curve and equivalent stress-strain curve for the hydraulic bulge test using Hill 1979 (red circles). For completeness, the bulge test (red open circles) and uniaxial tension (black open circles) experimental true stress-strain curves are overlaid.

The bulge test (red open circles) and uniaxial tension (black open circles) experimental data stress-strain curves are also included in Figure A1. Note that the bulge test experimental data is plotted in terms of true stress and strain not equivalent stress and strain. The material anisotropy is evident by the difference in the hardening behavior between these experimental true stress-strain curves.

### A.2. Cruciform Specimen Geometric Relationships

Through thickness geometric relationship (see Figure 9) for the flat gauge region results in,

$$T_{\text{cut}} = \frac{\left(T_{\text{sample}} - T_{\text{pocket}}\right)}{2} \tag{A2.1}$$

and

$$R_{\text{pocket}} = \begin{cases} \left(R_{\text{gauge}} + F_{\text{pocket}}\right), \text{if } F_{\text{pocket}} \leq T_{\text{cut}} \\ \left[R_{\text{gauge}} + \sqrt{F_{\text{pocket}}^2 - \left(F_{\text{pocket}} - T_{\text{cut}}\right)^2}\right], \text{if } F_{\text{pocket}} > T_{\text{cut}} \end{cases} \tag{A2.2}$$

See Figure A2a for more clarification on Eq. A2. Based on the authors' prior experience, $R_{\text{notch}}$ is determined by the following relationship with $W_{\text{arm}}$,

$$R_{\text{notch}} = \frac{W_{\text{arm}}}{6} \tag{A2.3}$$

Based on the geometric relationship in Figure 9a and Figure A2b,

$$W_{\text{arm}} \frac{\sqrt{2}}{2} = R_{\text{pocket}} + L_{\text{N2P}} + R_{\text{notch}} \tag{A2.4}$$

where $L_{\text{N2P}}$ is the shortest distance from the notch to the pocket along the diagonal direction. Substituting Eq. A3 into Eq. A4 and solving for $W_{\text{arm}}$,

$$W_{\text{arm}} = \left(R_{\text{pocket}} + L_{\text{N2P}}\right)\left(\frac{6}{3\sqrt{2} - 1}\right) \tag{A2.5}$$

Assuming that proper triaxial strain is obtained in the corner reinforcement by constraining a relative dimension of in-plane geometry and the sample thickness,

$$L_{\mathrm{N2P}} \geq T_{\mathrm{sample}} \tag{A2.6}$$

and therefore, the minimum of $W_{\mathrm{arm}}$ can be determined by the following equation.

$$W_{\mathrm{arm}} \geq \left(R_{\mathrm{pocket}} + T_{\mathrm{sample}}\right)\left(\frac{6}{3\sqrt{2}-1}\right) \tag{A2.7}$$

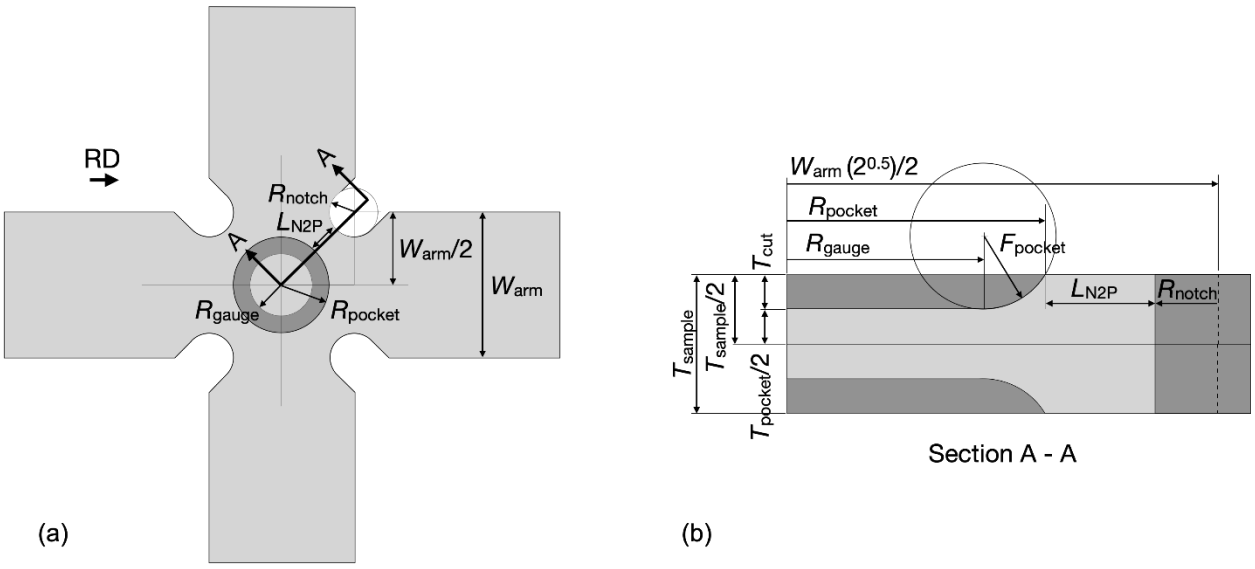


Figure A2. Relationship between the key geometric features for the design (a) plane view and (b) section A-A.

## References


[1] Hill R, Orowan E. A theory of the yielding and plastic flow of anisotropic metals. Proc R Soc Lond Ser Math Phys Sci 1948;193:281–97. https://doi.org/10.1098/rspa.1948.0045.

[2] Hosford WF. On yield loci of anisotropic cubic metals. Proc. Seventh North Am. Met. Work. Conf., SME; 1979, p. 191–7.
[3] Hershey AV. The Plasticity of an Isotropic Aggregate of Anisotropic Face-Centered Cubic Crystals. J Appl Mech 1954;21:241–9. https://doi.org/10.1115/1.4010900.
[4] Barlat F, Lian K. Plastic behavior and stretchability of sheet metals. Part I: A yield function for orthotropic sheets under plane stress conditions. Int J Plast 1989;5:51–66. https://doi.org/10.1016/0749-6419(89)90019-3.
[5] Karafillis AP, Boyce MC. A general anisotropic yield criterion using bounds and a transformation weighting tensor. J Mech Phys Solids 1993;41:1859–86. https://doi.org/10.1016/0022-5096(93)90073-O.
[6] Barlat F, Lege DJ, Brem JC. A six-component yield function for anisotropic materials. Int J Plast 1991;7:693–712. https://doi.org/10.1016/0749-6419(91)90052-Z.
[7] Barlat F, Maeda Y, Chung K, Yanagawa M, Brem JC, Hayashida Y, et al. Yield function development for aluminum alloy sheets. J Mech Phys Solids 1997;45:1727–63. https://doi.org/10.1016/S0022-5096(97)00034-3.
[8] Barlat F, Brem JC, Yoon JW, Chung K, Dick RE, Lege DJ, et al. Plane stress yield function for aluminum alloy sheets—part 1: theory. Int J Plast 2003;19:1297–319. https://doi.org/10.1016/S0749-6419(02)00019-0.
[9] Barlat F, Aretz H, Yoon JW, Karabin ME, Brem JC, Dick RE. Linear transfomation-based anisotropic yield functions. Int J Plast 2005;21:1009–39. https://doi.org/10.1016/j.ijplas.2004.06.004.
[10] Cazacu O, Barlat F. Generalization of Drucker's Yield Criterion to Orthotropy. Math Mech Solids 2001;6:613–30. https://doi.org/10.1177/108128650100600603.
[11] Cazacu O, Barlat F. Application of the theory of representation to describe yielding of anisotropic aluminum alloys. Int J Eng Sci 2003;41:1367–85. https://doi.org/10.1016/S0020-7225(03)00037-5.
[12] Bron F, Besson J. A yield function for anisotropic materials Application to aluminum alloys. Int J Plast 2004;20:937–63. https://doi.org/10.1016/j.ijplas.2003.06.001.
[13] Banabic D, Kuwabara T, Balan T, Comsa DS, Julean D. Non-quadratic yield criterion for orthotropic sheet metals under plane-stress conditions. Int J Mech Sci 2003;45:797–811. https://doi.org/10.1016/S0020-7403(03)00139-5.
[14] Banabic D, Aretz H, Comsa DS, Paraianu L. An improved analytical description of orthotropy in metallic sheets. Int J Plast 2005;21:493–512. https://doi.org/10.1016/j.ijplas.2004.04.003.
[15] Banabic D, Barlat F, Cazacu O, Kuwabara T. Advances in anisotropy and formability. Int J Mater Form 2010;3:165–89. https://doi.org/10.1007/s12289-010-0992-9.
[16] Barlat F, Kuwabara T. Anisotropic Yield Conditions in Mathematical Theory of Plasticity. J Jpn Soc Technol Plast 2016;57:230–43. https://doi.org/10.9773/sosei.57.230.
[17] Lee J, Bong HJ, Ha J, Choi J, Lee M-G, Barlat F. Influence of Yield Stress Determination in Anisotropic Hardening Model on Springback Prediction in Dual-Phase Steel. JOM 2018;70. https://doi.org/10.1007/s11837-018-2910-4.
[18] Ha J, Baral M, Korkolis YP. Plastic anisotropy and ductile fracture of bake-hardened AA6013 aluminum sheet. Int J Solids Struct 2018;155:123–39. https://doi.org/10.1016/j.ijsolstr.2018.07.015.

[19] Ha J, Coppieters S, Korkolis YP. On the expansion of a circular hole in an orthotropic elastoplastic thin sheet. Int J Mech Sci 2020;182:105706. https://doi.org/10.1016/j.ijmecsci.2020.105706.
[20] Choi Y, Ha J, Lee M-G, Korkolis YP. Effect of plastic anisotropy and Portevin-Le Chatelier bands on hole-expansion in AA7075 sheets in -T6 and -W tempers. J Mater Process Technol 2021;296:117211. https://doi.org/10.1016/j.jmatprotec.2021.117211.
[21] Ha J, Korkolis YP. Hole-Expansion: Sensitivity of Failure Prediction on Plastic Anisotropy Modeling. J Manuf Mater Process 2021;5:28. https://doi.org/10.3390/jmmp5020028.
[22] Ha J, Kim J-H, Barlat F, Lee M-G. Continuous strain path change simulations for sheet metal. Comput Mater Sci 2014;82:286–92. https://doi.org/10.1016/j.commatsci.2013.09.042.
[23] Lee J, Ha J, Bong HJ, Kim D, Lee M-G. Evolutionary anisotropy and flow stress in advanced high strength steels under loading path changes. Mater Sci Eng A 2016;672:65–77. https://doi.org/10.1016/j.msea.2016.06.074.
[24] Ha J, Lee J, Kim JH, Lee M-G, Barlat F. Investigation of plastic strain rate under strain path changes in dual-phase steel using microstructure-based modeling. Int J Plast 2017;93:89–111. https://doi.org/10.1016/j.ijplas.2017.02.005.
[25] Kuwabara T, Mori T, Asano M, Hakoyama T, Barlat F. Material modeling of 6016-O and 6016-T4 aluminum alloy sheets and application to hole expansion forming simulation. Int J Plast 2017;93:164–86. https://doi.org/10.1016/j.ijplas.2016.10.002.
[26] Chaboche JL. Time-independent constitutive theories for cyclic plasticity. Int J Plast 1986;2:149–88. https://doi.org/10.1016/0749-6419(86)90010-0.
[27] Yoshida F, Uemori T, Fujiwara K. Elastic–plastic behavior of steel sheets under in-plane cyclic tension–compression at large strain. Int J Plast 2002;18:633–59. https://doi.org/10.1016/S0749-6419(01)00049-3.
[28] Chung K, Lee M-G, Kim D, Kim C, Wenner ML, Barlat F. Spring-back evaluation of automotive sheets based on isotropic-kinematic hardening laws and non-quadratic anisotropic yield functions: Part I: theory and formulation. Int J Plast 2005;21:861–82. https://doi.org/10.1016/j.ijplas.2004.05.016.
[29] Barlat F, Gracio JJ, Lee M-G, Rauch EF, Vincze G. An alternative to kinematic hardening in classical plasticity. Int J Plast 2011;27:1309–27. https://doi.org/10.1016/j.ijplas.2011.03.003.
[30] Barlat F, Ha J, Grácio JJ, Lee M-G, Rauch EF, Vincze G. Extension of homogeneous anisotropic hardening model to cross-loading with latent effects. Int J Plast 2013;46:130–42. https://doi.org/10.1016/j.ijplas.2012.07.002.
[31] Barlat F, Vincze G, Grácio JJ, Lee M-G, Rauch EF, Tomé CN. Enhancements of homogenous anisotropic hardening model and application to mild and dual-phase steels. Int J Plast 2014;58:201–18. https://doi.org/10.1016/j.ijplas.2013.11.002.
[32] Kuwabara T, Hashimoto K, Iizuka E, Yoon JW. Effect of anisotropic yield functions on the accuracy of hole expansion simulations. J Mater Process Technol 2011;211:475–81. https://doi.org/10.1016/j.jmatprotec.2010.10.025.
[33] Deng N, Kuwabara T, Korkolis YP. On the non-linear unloading behavior of a biaxially loaded dual-phase steel sheet. Int J Mech Sci 2018;138–139:383–97. https://doi.org/10.1016/j.ijmecsci.2018.02.015.

[34] Yoon J-W, Barlat F, Dick RE, Chung K, Kang TJ. Plane stress yield function for aluminum alloy sheets—part II: FE formulation and its implementation. Int J Plast 2004;20:495–522. https://doi.org/10.1016/S0749-6419(03)00099-8.
[35] Yoon J, Barlat F, Dick R, Karabin M. Prediction of six or eight ears in a drawn cup based on a new anisotropic yield function 2006. https://doi.org/10.1016/J.IJPLAS.2005.03.013.
[36] Ha J, Baral M, Korkolis YP. Ductile fracture of an aluminum sheet under proportional loading. J Mech Phys Solids 2019;132:103685. https://doi.org/10.1016/j.jmps.2019.103685.
[37] Ha J, Fones J, Kinsey BL, Korkolis YP. Plasticity and Formability of Annealed, Commercially-Pure Aluminum: Experiments and Modeling. Materials 2020;13:4285. https://doi.org/10.3390/ma13194285.
[38] Baral M, Hama T, Knudsen E, Korkolis YP. Plastic deformation of commercially-pure titanium: experiments and modeling. Int J Plast 2018;105:164–94. https://doi.org/10.1016/j.ijplas.2018.02.009.
[39] Ishiki M, Kuwabara T, Hayashida Y. Measurement and analysis of differential work hardening behavior of pure titanium sheet using spline function. Int J Mater Form 2011;4:193–204. https://doi.org/10.1007/s12289-010-1024-5.
[40] Nagano C, Kuwabara T, Shimada Y, Kawamura R. Measurement of Differential Hardening under Biaxial Stress of Pure Titanium Sheet. IOP Conf Ser Mater Sci Eng 2018;418:012090. https://doi.org/10.1088/1757-899X/418/1/012090.
[41] Steglich D, Jeong Y, Andar MO, Kuwabara T. Biaxial deformation behaviour of AZ31 magnesium alloy: Crystal-plasticity-based prediction and experimental validation. Int J Solids Struct 2012;49:3551–61. https://doi.org/10.1016/j.ijsolstr.2012.06.017.
[42] Steglich D, Tian X, Bohlen J, Kuwabara T. Mechanical Testing of Thin Sheet Magnesium Alloys in Biaxial Tension and Uniaxial Compression. Exp Mech 2014;54:1247–58. https://doi.org/10.1007/s11340-014-9892-0.
[43] Mamros EM, Ha J, Korkolis Y, Kinsey B. Experimental Investigation and Plasticity Modeling of SS316L Microtubes Under Varying Deformation Paths. J Micro Nano-Manuf 2020. https://doi.org/10.1115/1.4049364.
[44] Creuziger A, Iadicola MA, Foecke T, Rust E, Banerjee D. Insights into Cruciform Sample Design. JOM 2017;69:902–6. https://doi.org/10.1007/s11837-017-2261-6.
[45] Ha J, Lee M-G, Barlat F. Strain hardening response and modeling of EDDQ and DP780 steel sheet under non-linear strain path. Mech Mater 2013;64:11–26. https://doi.org/10.1016/j.mechmat.2013.04.004.
[46] Tozawa Y. Plastic Deformation Behavior under Conditions of Combined Stress. In: Koistinen DP, Wang N-M, editors. Mech. Sheet Met. Form. Mater. Behav. Deform. Anal., Boston, MA: Springer US; 1978, p. 81–110. https://doi.org/10.1007/978-1-4613-2880-3_4.
[47] Upadhyay MV, Patra A, Wen W, Panzner T, Van Petegem S, Tomé CN, et al. Mechanical response of stainless steel subjected to biaxial load path changes: Cruciform experiments and multi-scale modeling. Int J Plast 2018;108:144–68. https://doi.org/10.1016/j.ijplas.2018.05.003.
[48] Brünig M, Gerke S, Schmidt M. Biaxial experiments and phenomenological modeling of stress-state-dependent ductile damage and fracture. Int J Fract 2016;200:63–76. https://doi.org/10.1007/s10704-016-0080-3.

[49] Brünig M, Schmidt M, Gerke S. Numerical analysis of stress-state-dependent damage and failure behavior of ductile steel based on biaxial experiments. Comput Mech 2021;68:1–11. https://doi.org/10.1007/s00466-020-01932-z.
[50] Shiratori E, Ikegami K. A New Biaxial Tension Testing Machine with Flat Specimens. J Soc Mater Sci Jpn 1967;16:433–9. https://doi.org/10.2472/jsms.16.433.
[51] Kuwabara T, Ikeda S, Kuroda K. Measurement and analysis of differential work hardening in cold-rolled steel sheet under biaxial tension. J Mater Process Technol 1998;80–81:517–23. https://doi.org/10.1016/S0924-0136(98)00155-1.
[52] International Organization for Standardization. Metallic materials — Sheet and strip — Biaxial tensile testing method using a cruciform test piece (ISO 16842). ISO 2014.
[53] Hanabusa Y, Takizawa H, Kuwabara T. Evaluation of Accuracy of Stress Measurements Determined in Biaxial Stress Tests with Cruciform Specimen Using Numerical Method. Met Form 2010:5.
[54] Hanabusa Y, Takizawa H, Kuwabara T. Numerical verification of a biaxial tensile test method using a cruciform specimen. J Mater Process Technol 2013;213:961–70. https://doi.org/10.1016/j.jmatprotec.2012.12.007.
[55] Coppieters S, Hakoyama T, Yanaga D, Lava P, Kuwabara T. On stress measurement errors in biaxial tensile testing and the impact on yield surface identification. AIP Conf Proc 2013;1567:628. https://doi.org/10.1063/1.4850051.
[56] Banerjee DK, Iadicola MA, Creuziger AA, Foecke TJ. An Experimental and Numerical Study of Deformation Behavior of Steels in Biaxial Tensile Tests. Miner Met Mater Soc Eds TMS 2015 144th Annu Meet Exhib 2015. https://doi.org/10.1007/978-3-319-48127-2_35.
[57] Giannella V, Dhondt G, Kontermann C, Citarella R. Combined static-cyclic multi-axial crack propagation in cruciform specimens. Int J Fatigue 2019;123:296–307. https://doi.org/10.1016/j.ijfatigue.2019.02.029.
[58] Gerke S, Adulyasak P, Brünig M. New biaxially loaded specimens for the analysis of damage and fracture in sheet metals. Int J Solids Struct 2017;110–111:209–18. https://doi.org/10.1016/j.ijsolstr.2017.01.027.
[59] Deng N, Kuwabara T, Korkolis YP. Cruciform Specimen Design and Verification for Constitutive Identification of Anisotropic Sheets. Exp Mech 2015;55:1005–22. https://doi.org/10.1007/s11340-015-9999-y.
[60] Hou Y, Min J, Lin J, Carsley JE, Stoughton TB. Cruciform specimen design for large plastic strain during biaxial tensile testing. J Phys Conf Ser 2018;1063:012160. https://doi.org/10.1088/1742-6596/1063/1/012160.
[61] Zhao K, Chen L, Xiao R, Ding Z, Zhou L. Design of a biaxial tensile testing device and cruciform specimens for large plastic deformation in the central zone. J Mater Sci 2019;54:7231–45. https://doi.org/10.1007/s10853-019-03358-2.
[62] Hannon A, Tiernan P. A review of planar biaxial tensile test systems for sheet metal. J Mater Process Technol 2008;198:1–13. https://doi.org/10.1016/j.jmatprotec.2007.10.015.
[63] Murakoso S, Kuwabara T. Measurement and Analysis of Ultra-Thin Austenitic Stainless Steel Sheet under Biaxial Tensile Loading and In-Plane Reverse Loading. J Solid Mech Mater Eng 2009;3:1330–9. https://doi.org/10.1299/jmmp.3.1330.

[64] Zhang R, Shao Z, Shi Z, Dean TA, Lin J. Effect of cruciform specimen design on strain paths and fracture location in equi-biaxial tension. J Mater Process Technol 2021;289:116932. https://doi.org/10.1016/j.jmatprotec.2020.116932.
[65] Mamros EM, Eaton MC, Ha J, Kinsey BL. Numerical Analysis of SS316L Biaxial Cruciform Specimens Under Proportional Loading Paths. Proc. ASME Manuf. Sci. Eng. Conf., Virtual: ASME; 2021. https://doi.org/10.1115/MSEC2021-59877.
[66] Mamros EM, Mayer SM, Ha J, Kinsey BL. Experimental Implementation of SS 316L Cruciform Testing to Achieve Various Deformation Paths. In: Daehn G, Cao J, Kinsey B, Tekkaya E, Vivek A, Yoshida Y, editors. Form. Future, Cham: Springer International Publishing; 2021, p. 1981–90. https://doi.org/10.1007/978-3-030-75381-8_166.
[67] Andar M, Kuwabara T, Yonemura S, Uenishi A. Elastic–Plastic and Inelastic Characteristics of High Strength Steel Sheets under Biaxial Loading and Unloading. Isij Int - ISIJ INT 2010;50:613–9. https://doi.org/10.2355/isijinternational.50.613.
[68] Kim M, Ha J, Bonica S, Korkolis YP. Design of a New Cruciform-Like Specimen for Combined Tension and Shear of Metal Sheets. In: Daehn G, Cao J, Kinsey B, Tekkaya E, Vivek A, Yoshida Y, editors. Form. Future, Cham: Springer International Publishing; 2021, p. 1961–7. https://doi.org/10.1007/978-3-030-75381-8_164.
[69] Kuwabara T, Ikeda S. Plane-strain tension test of steel sheet using servo-controlled biaxial tensile testing machine 2002.
[70] Demmerle S, Boehler JP. Optimal design of biaxial tensile cruciform specimens. J Mech Phys Solids 1993;41:143–81. https://doi.org/10.1016/0022-5096(93)90067-P.
[71] Leotoing L, Guines D, Zhang SY, Ragneau E. A Cruciform Shape to Study the Influence of Strain Paths on Forming Limit Curves. Key Eng Mater 2013;554–557:41–6. https://doi.org/10.4028/www.scientific.net/KEM.554-557.41.
[72] Leotoing L, Guines D, Zidane I, Ragneau E. Cruciform shape benefits for experimental and numerical evaluation of sheet metal formability. J Mater Process Technol 2013;213:856–63. https://doi.org/10.1016/j.jmatprotec.2012.12.013.
[73] Kuwabara T, Tachibana R, Takada Y, Koizumi T, Coppieters S, Barlat F. Effect of hydrostatic stress on the strength differential effect in low-carbon steel sheet | SpringerLink n.d. https://link.springer.com/article/10.1007/s12289-022-01650-2 (accessed June 27, 2022).
[74] Takada Y, Kuwabara T. Nonlinear biaxial tensile stress path experiment without intermediate elastic unloading for validation of material model. Int J Solids Struct 2022:111777. https://doi.org/10.1016/j.ijsolstr.2022.111777.
[75] ASTM. ASTM E8/E8M-16a Standard Test Methods for Tension Testing of Metallic Materials. ASTM Standards 2013;03.01. https://doi.org/10.1520/E0008-04.
[76] Hill R. C. A theory of the plastic bulging of a metal diaphragm by lateral pressure. Lond Edinb Dublin Philos Mag J Sci 1950;41:1133–42. https://doi.org/10.1080/14786445008561154.
[77] Johnson W, Duncan JL. The use of the biaxial test extensometer. Sheet Met Ind 1965;42:271–5.
[78] Yoshida K. Evaluation of Stress and Strain Measurement Accuracy in Hydraulic Bulge Test with the Aid of Finite-element Analysis. ISIJ Int 2013;53:86–95. https://doi.org/10.2355/isijinternational.53.86.

[79] Hockett JE, Sherby OD. Large strain deformation of polycrystalline metals at low homologous temperatures. J Mech Phys Solids 1975;23:87–98. https://doi.org/10.1016/0022-5096(75)90018-6.
[80] Hill R. Theoretical plasticity of textured aggregates. Math Proc Camb Philos Soc 1979;85:179–91. https://doi.org/10.1017/S0305004100055596.
[81] Wagoner RH. Measurement and analysis of plane-strain work hardening. Metall Mater Trans A 1980;11:165–75. https://doi.org/10.1007/BF02700453.
[82] Hosford WF. A Generalized Isotropic Yield Criterion. J Appl Mech 1972;39:607–9. https://doi.org/10.1115/1.3422732.
[83] Logan RW, Hosford WF. Upper-bound anisotropic yield locus calculations assuming <111>-pencil glide 1980:12.
[84] Mamros EM, Kuijer MB, Davarpanah MA, Baker I, Kinsey BL. The Effect of Temperature on the Strain-Induced Austenite to Martensite Transformation in SS 316L During Uniaxial Tension. In: Daehn G, Cao J, Kinsey B, Tekkaya E, Vivek A, Yoshida Y, editors. Form. Future, Cham: Springer International Publishing; 2021, p. 1853–62. https://doi.org/10.1007/978-3-030-75381-8_155.
[85] Feng Z, Mamros EM, Ha J, Kinsey BL, Knezevic M. Modeling of plasticity-induced martensitic transformation to achieve hierarchical, heterogeneous, and tailored microstructures in stainless steels. CIRP J Manuf Sci Technol 2021;33:389–97. https://doi.org/10.1016/j.cirpj.2021.04.006.
[86] ABAQUS 2019.
[87] Wilkins ML. Calculation of Elastic-Plastic Flow. California University Livermore Radiation Lab; 1963.
[88] Ortiz M, Simo JC. An analysis of a new class of integration algorithms for elastoplastic constitutive relations. Int J Numer Methods Eng 1986;23:353–66. https://doi.org/10.1002/nme.1620230303.
[89] Cardoso RPR, Yoon JW. Stress integration method for a nonlinear kinematic/isotropic hardening model and its characterization based on polycrystal plasticity. Int J Plast 2009;25:1684–710. https://doi.org/10.1016/j.ijplas.2008.09.007.
[90] Isight 2019.
[91] Wilson JF, Kinsey BL, Korkolis YP. Development of a biaxial loading frame for sheet metal. J Manuf Process 2013;15:580–5. https://doi.org/10.1016/j.jmapro.2013.06.008.
[92] Deng N, Gagnon I, Kubec V, Kinsey BL, Korkolis YP. Biaxial loading of anisotropic Al-6022-T4 sheets using cruciform specimens 2016.